



A combined experimental/numerical study on the scaling of impact strength and toughness in composite laminates for ballistic applications

Stefano Signetti^{a,b}, Federico Bosia^c, Seunghwa Ryu^b, Nicola M. Pugno^{a,d,*}

^a Laboratory of Bio-Inspired, Bionic, Nano, Meta Materials & Mechanics, Department of Civil, Environmental and Mechanical Engineering, University of Trento, via Mesiano 77, I-38123, Trento, Italy

^b Department of Mechanical Engineering, Korea Advanced Institute of Science and Technology, 291 Daehak-ro, Yuseong-gu, Daejeon, 34141, Republic of Korea

^c Department of Applied Science and Technology, Politecnico di Torino, corso Duca degli Abruzzi, 10129, Torino, Italy

^d School of Engineering and Materials Science, Queen Mary University of London, Mile End Road E1 4NS, London, United Kingdom

ARTICLE INFO

Keywords:

Composite laminates
Multiscale characterization
Finite element simulations
Impact strength
Toughness

ABSTRACT

In this paper, the impact behaviour of composite laminates is investigated, and their potential for ballistic protection assessed, as a function of the reinforcing materials and structures for three representative fibre-reinforced epoxy systems involving carbon, glass, or para-aramid fibre reinforcements, respectively. A multiscale coupled experimental/numerical study on the composite material properties is performed, starting from single fibre, to fibre bundles (yarns), to single composite ply, and finally at laminate level. Uniaxial tensile tests on single fibres and fibre bundles are performed, and the results are used as input for non-linear Finite Element Method (FEM) models for tensile and impact simulation on the composite laminates. Mechanical properties and energy dissipation of the single ply and multilayer laminates under quasi-static loading are preliminarily assessed starting from the mechanical properties of the constituents and subsequently verified numerically. FEM simulations of ballistic impact on multilayer armours are then performed, assessing the three different composites, showing good agreement with experimental tests in terms of impact energy absorption capabilities and deformation/failure behaviour. As result, a generalized multiscale version of the well-known Cuniff criterion is provided as a scaling law, which allows to assess the ballistic performance of laminated composites, starting from the tensile mechanical properties of the fibres and fibre bundles and their volume fraction. The presented multiscale coupled experimental-numerical characterization confirms the reliability of the predictions for full-scale laminate properties starting from the individual constituents at the single fibre scale.

1. Introduction

One of the main challenges in the development of protective armours against high-velocity impacts is to maximize the protection levels using lightweight materials and structures, since for many applications the use of large masses may be impractical or unsuitable, such as in aerospace applications. Conventional armours made with metal alloys or ceramic materials have been widely used in the past, with the latter guaranteeing comparable protection levels at almost a third of the weight of metals [1]. Armours made from these materials are isotropic, and their capability of stopping ballistic projectiles is proportional to the mass of the target, so that either the required minimum density or the thickness may become large for extreme protection levels. Therefore, these solutions

are not applicable where low weight is fundamental to ensure unrestricted and efficient mobility, e.g. in terrestrial vehicles, aircraft, and spacecraft, or when material flexibility is desirable to guarantee ergonomics to body armour, such as for defense or sports applications [2].

In this regard, composite materials based on high performance fibre reinforcements exhibit high specific strength and stiffness [3–5], allowing the fabrication of relatively thin and flexible armours with good corrosion resistance [6]. These composites have good damage tolerance [6,7] and fatigue properties [8], as well as excellent thermal and acoustic insulation [9]. They are also easy to fabricate, reducing costs and allowing flexibility in design [7,9,10], providing access to a combination of a wide range of materials that enable optimization for specific purposes. Another important characteristic is the limited

* Corresponding author. Laboratory of Bio-Inspired, Bionic, Nano, Meta Materials & Mechanics, Department of Civil, Environmental and Mechanical Engineering, University of Trento, via Mesiano 77, I-38123, Trento, Italy.

E-mail address: nicola.pugno@unitn.it (N.M. Pugno).

<https://doi.org/10.1016/j.compositesb.2020.108090>

Received 23 September 2019; Received in revised form 6 April 2020; Accepted 19 April 2020

Available online 25 April 2020

1359-8368/© 2020 Elsevier Ltd. All rights reserved.

degradation of properties after multiple impact events, i.e. the damage tolerance, which determines the long-term survivability of protective systems in harsh environments [6].

Armour protective capabilities are usually assessed in the terminal ballistics community on the basis of the so called V_{50} parameter, i.e. the velocity corresponding to a 50% probability that the impacting mass is stopped by the target without perforation. According to the dimensional analysis carried out by Cuniff [11] for an elastic textile barrier, made of fibres of density ρ , tensile strength σ , Young's modulus E , and failure strain ε , is $V_{50} \sim U^{1/3}$, where $U = \frac{\sigma \varepsilon}{2\rho} \sqrt{\frac{E}{\rho}}$ is a parameter obtained as the product of the material-specific dissipated energy and the acoustic wave speed in the considered fibres. This dimensional analysis allows to compare the actual protective performance of a wide range of fabrics. The advantage of employing composites over traditional metals and ceramics to increase the impact toughness clearly emerges due to their lower density, as well as higher strain to failure, specific strength and stiffness [3]. The good prediction capability of the above scaling criterion is an indication that fibre failure, both in tension and in shear due to shear plug [5], is one of the main damage mechanisms in multilayer composite armours, and it is thus the primary source of energy absorption. Other principal damage mechanisms involve inter-layer delamination [12], matrix cracking and melting [13], fibre-matrix debonding, and fibre spallation [14]. However, the above mentioned criterion does not account for the actual complexity of composites, where volume fraction, different fibre orientation among different layers, and most of all size-scale effects of material properties play a role.

Reinforcing fibres employed in composites are usually assembled in unidirectional or bidirectional woven fabrics, in the form of dry preforms or pre-impregnated with resin, in order to guarantee their uniform distribution and an even load transfer within the matrix [3,15]. Short fibre reinforcements and random distributed long fibre mats are usually not suitable for ballistic applications due to their non-uniform microstructures. Woven fabrics are formed by interlacing two or more sets of bundle (yarns). Plain woven fabric is the simplest biaxial woven preform. More sets of yarns can also be used, and the resulting fabrics are called triaxial or multiaxial weaves, with progressively increasing grades of isotropy of mechanical properties of the fabric and of the resulting composite ply [16]. On the other hand, these architectures usually result in less compacted composite laminates with lower volume fractions with respect to bidirectional plain weaves, resulting in lower ballistic strength [17,18].

The complex mechanical behaviour emerging in laminate response, due to the presence of microscopic to macroscopic characteristic scales, requires a multiscale description from single fibre, to bundle, to ply and finally to laminate level for the selection of the optimal constituents and configurations for ballistic applications. Theoretical and computational methods can provide new insights in the comprehension of fracture mechanisms and of scaling of mechanical properties in heterogeneous/hierarchical/multiscale structures, beginning from micro-scale. One example of fibrous materials models is represented by so-called Hierarchical Fibre Bundle Models (HFBM) [19,20] where the mechanical properties of a fibre or thread at a given hierarchical level are statistically inferred from the average output deriving from repeated simulations at the lower level, down to the lowest hierarchical level, allowing the simulation of multiscale or hierarchical structures. Results show that specific hierarchical organizations can lead to increased damage resistance (e.g., self-similar fibre reinforced matrix materials) or that the interaction between hierarchy and material heterogeneity is critical, since homogeneous hierarchical bundles do not exhibit improved properties [21].

Moving up to the composite level, numerous theories have been proposed to date to describe the kinematics and stress states of composite laminates. Most of these laminate theories are extensions of the conventional, single-layer plate theories (e.g. Reissner-Mindlin [22,23]) which are based on assumed variation of either stresses or displacements

through the plate thickness. Equivalent Single Layer theories (ESL) [24–26] are simple extension of single layer theories accounting for variable sub-thickness and material properties in the solutions of partial differential equations of the single layer homogeneous plate. In carrying out the integration, it is assumed that the layers are perfectly bonded. For many applications, the ESL theories provide a sufficiently accurate description of the global laminate response, e.g. tensile properties, transverse deflection, natural vibrations, critical buckling load. The main advantages of the ESL models are their inherent simplicity and low computational cost due to the relatively small number of variables. However, they are often inadequate for determining the three-dimensional stress field at the ply level, which may arise from severe bending or highly localized contact pressure. Moreover, the main shortcoming of the ESL models in modelling composite laminates is that the transverse strain components are continuous across interfaces between dissimilar (variable stiffness) materials. Unlike the ESL theories, layer-wise (or laminate shell) theories [27,28] assume separate displacement field expansions within each material layer, thus providing a kinematically consistent representation of the strain field in discrete layer laminates, and allowing accurate determination of stresses within single plies. Such laminate theories are currently implemented in the most advanced element formulations in non-linear Finite Element Method (FEM) codes [25].

Nowadays, these FEM approaches are capable of modelling the main mechanical phenomena which occur in high-velocity impact events such as contact, inter-layer delamination, material fracture and fragmentation, allowing the accurate replication of ballistic tests and their partial substitution in the design and optimization process [12,29–31]. Such codes include sophisticated constitutive models, also accounting for strain-rate effects, and anisotropic failure criteria that allow the modelling of the most complex materials. In this regard, the accuracy and prediction capabilities in the design process of such models relies, at first, on the accurate characterization of material properties, which should be based on a multiscale approach. This would be fundamental, along with the identification to key target parameters, for the application of machine learning techniques to optimize composites [32].

In this paper, we investigate the impact behaviour of three types of epoxy composite laminates reinforced with carbon, E-glass, and Twaron® (para-aramid, PA) fibres, respectively, and assess their potential for ballistic protection as a function of their structure and constitutive components. To the best of the authors' knowledge, similar studies so far, also very recent, have been limited to low velocity impacts or have not included a systematic investigation across all the dimensional scales involved [33,34]. The aim is to create a simple multiscale characterization protocol that exploits the properties extracted from the single components at the micro-scale as input for reliable impact simulations at the macro-scale. First, the tensile properties of single fibres and of the bundles (yarns) constituting the orthotropic woven textiles are characterized. Then, the obtained properties are used as input for FEM simulations to replicate tensile experiments on the laminates. Scaling of mechanical properties of interest with the characteristic sample size is also assessed. Finally, FEM impact simulations are performed to replicate experimental ballistic tests (initial projectile velocity $V_0 \cong 360$ m/s, impact kinetic energy $K_0 \cong 520$ J) on armours constituted by the previously characterized plies, computing their absorption capabilities and deformation/failure behaviour. The good agreement of impact simulation and ballistic experiments proves the validity of the proposed multiscale coupled experimental-simulation method. Finally, a multiscale generalization of the Cuniff parameter is proposed to rationalize the results, providing a relatively simple scaling law that allows to assess and predict the ballistic performance of laminated composites, starting from the tensile mechanical properties of the fibres, their volume fraction and arrangement, which can provide preliminary design criteria with related time cost reductions in terms of prototyping and experimental tests.

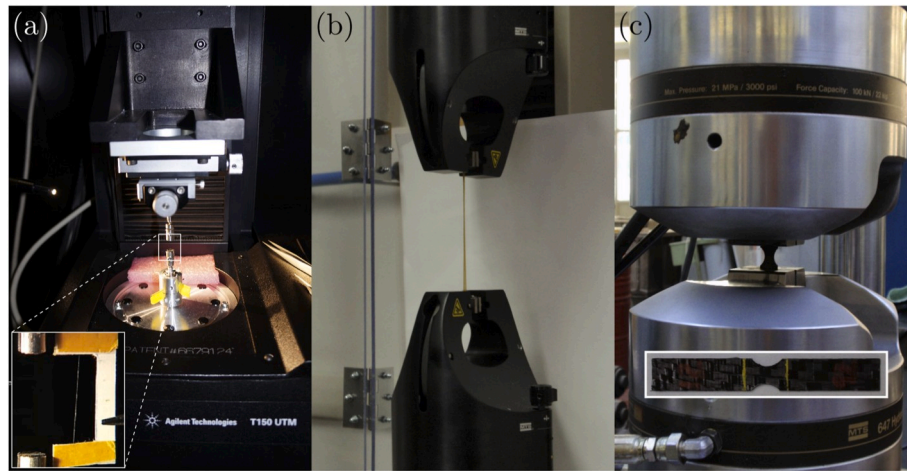


Fig. 1. Material multiscale experimental characterization. (a) Micro-tensile characterization of single fibres (the inset illustrates the “C-shaped” frame for placement of the single fibre in the loading cell); (b) meso-scale characterization of fibre bundles extracted from the textiles; (c) macro-tensile characterization of laminates (a typical carbon sample is shown in the inset).

2. Materials and methods

2.1. Characterization of fibres, bundles and laminates

We consider three of the most widely used fibre types in the manufacture of high-strength composites: carbon (T800), E-glass, and PA. The fibres were extracted from woven textile samples manufactured by G. Angeloni s.r.l., Italy, and commercially identified as fabrics *GG 301 T8*, *VV-300 P*, and *Style 281*, respectively.

First, single fibres were tested under uniaxial tension [35] using an Agilent T150 Nanotensile testing system (Fig. 1a), which allows sensitivity down to nN and nm on loads and displacements, respectively. 5 tests per fibre type were conducted. The samples, with a typical gauge length of 20 mm, were prepared in “C-shaped” paper frames and set-up in a clamped-clamped configuration in the sample holder (Fig. 1a). The paper frame is then cut and fibres loaded up to failure at a loading rate of 1 mm/min. The micro-fibres are analysed before and after testing using a Scanning Electron Microscope (SEM) to measure exact diameters. The fibre reinforcements for the considered laminated composites, in the form of fibre yarns, are arranged in “plain weave” configuration, i.e. constituted by woven fibre bundles in mutually orthogonal directions (“weft” and “warp”, see Figure S1 in the Supplementary Information). Given the non-uniformity in thickness and in density of the yarns and the uncertainty in the experimental determination of their actual thickness, the characterization is carried out on single fibre bundles with equivalent thickness properties. The experimental tests (5 tests per fibre type, due to high reproducibility of results) are performed after having measured the length l (distance between clamps) and mass m of the bundles and derived its cross-section area as $A = m/(l\rho)$, where ρ is the

volumetric bulk density of the corresponding material. The determined bundle cross-section areas are consistent with the values derived from the ratio between the linear density provided by the producers’ specifications (in dtex, = 10^{-7} kg/m) and the known volumetric density of the materials. Force-displacement ($F - \delta$) curves are measured using a MTS uniaxial testing system (with a 1 kN load cell, Fig. 1b), and converted to stress ($\sigma = F/A$)-strain ($\varepsilon = \delta/l$) curves. From these quantities, Young’s modulus $E = \sigma/\varepsilon$, fracture strength ($\sigma_f = \max\{\sigma\}$), and ultimate strain ($\varepsilon_f = \max\{\varepsilon\}$) are derived. The load application velocity is 1 mm/min.

Mechanical tests are also performed on laminated composite specimens [36] fabricated by Vemar s.r.l, Italy with the above textiles. The used resin is a thermoset *Bakelite® EPR L 1000 - set* by Bakelite AG. Single ply, 5-ply and 10-ply specimens are considered, with 0° and 45° orientation of the textile warp with respect to the loading direction. The different thicknesses and fibre orientations are considered to provide data for general conclusions, independent of the specific considered geometry. Specimen dimensions have a length of 10 cm and width of 15 mm. Small circular cuts (9 mm radius) are performed in the central part of the samples to prepare dog-bone specimens (Fig. 1.c and Supplementary Figure S2). Four specimen for each material/thickness/orientation subgroup are tested. Average thickness and volume fractions of the single and multilayer plies are reported in Table 1 (see Table S1 in the Supplementary information for further dimensional characteristics). The tests are performed using another MTS uniaxial testing system, with a 10 kN load cell (Fig. 1c) and a loading rate of 1 mm/min.

Table 1

Average ply thickness t and fibre volume fraction f (and related standard deviation) of the carbon, E-glass, and PA fibre-based composites with 1, 5, 10 layers at 0° and 45° orientation with respect to the direction of load application. The volume fraction f is determined assuming average textile thickness of 0.12 mm, 0.12 mm, and 0.10 mm for carbon, E-glass, and PA woven textiles, respectively, as specified from the producers. Data for all tested samples for each category are reported in full in Table S1 in the Supplementary Information.

	0°						45°					
	1 layer		5 layers		10 layers		1 layers		5 layer		10 layers	
	t [mm]	f										
Carbon	0.278 ± 0.0083	0.432 ± 0.0128	0.254 ± 0.218	0.473 ± 0.0381	0.270 ± 0.0187	0.444 ± 0.0326	0.298 ± 0.0083	0.403 ± 0.0111	0.257 ± 0.1139	0.468 ± 0.0392	0.235 ± 0.0500	0.511 ± 0.0109
Glass	0.275 ± 0.0433	0.406 ± 0.0866	0.185 ± 0.0087	0.649 ± 0.0289	0.178 ± 0.0043	0.676 ± 0.0170	0.325 ± 0.0433	0.369 ± 0.0433	0.240 ± 0.2121	0.500 ± 0.0874	0.181 ± 0.0249	0.664 ± 0.0092
PA	0.225 ± 0.0433	0.533 ± 0.0722	0.185 ± 0.0087	0.649 ± 0.0241	0.263 ± 0.0083	0.457 ± 0.0122	0.300 ± 0.0707	0.400 ± 0.0908	0.175 ± 0.0433	0.686 ± 0.0301	0.243 ± 0.1090	0.495 ± 0.0181

2.2. FEM tensile simulations

Dog-bone shaped laminate samples (geometrical characteristics are shown in Figure S2 in the Supplementary Information) have been reproduced in a FEM model to evaluate the capability of capturing the elastic and fracture behaviour of laminates via numerical simulation and comparing them with the results of experimental measurements and with approximate predictions by a rule of mixtures. The LS-DYNA® v971 R10.1 solver by Livermore Software Technology Corporation (LSTC) [37] was used in this study. 8 node solid-shell (also “thick-shell”) elements based on the Reissner-Mindlin kinematic assumption [22,23] and developed by Liu et al. [38] were employed for the simulations. This element formulation (TSHELL ELFORM = 1 [37]) allows the implementation of the laminate shell theories for an accurate computation of transversal stresses within the ply. A single point reduced in-plane integration rule was adopted. Although higher order in-plane integration schemes, e.g. 2x2 Gauss quadrature, could be chosen, we opted for this formulation since lower-order integration schemes are the most robust when element become largely distorted, as may happen in high-velocity impact simulations. Thus, we opted to use the same formulation in tensile simulation tests as that used in the more critical impact simulations presented later. Since single point quadrature is related to a reduction of the stiffness matrix, spurious zero-energy modes of deformation (also known as *hourglass* modes) may arise, as usually occurs under concentrated pressures. A viscous form hourglass control [39], i.e. introducing a fictitious viscosity, was used in the simulations (LS-DYNA hourglass type 3 [35]). We checked the fictitious energy introduced to mitigate hourglassing to be below 5% of the deformation energy at each simulation time for the whole model and for each of its deformable subparts (single plies). The ply thickness t and volume fraction f associated with each of the simulated cases were determined according to the measurements on experimental laminates (see Table 1). One single element through the thickness was used to model the single plies. Given the variable thickness of the plies of the various tested specimens (Table 1), the aspect ratios for the elements in the notched part of the specimens vary in ranges from $\sim 1:1:0.68$ (x, y, z) to $\sim 1:1:1.25$, with an in-plane characteristic size of about 0.26 mm (see Figure S2 in the Supplementary Information), as results from the performed convergence study (see Section S2.1 in the Supplementary Information). The thick shell element was sampled with 14 integration points (IPs) through the thickness, of which the 6 innermost were associated to the core of woven textile, while the outermost (4 + 4) were attributed to the epoxy matrix. The resulting integration scheme for all 18 simulated laminates is summarized in Table S3 in the Supplementary Information. MAT 58 (LAMINATED_COMPOSITE_FABRIC [37]) was used to simulate the fabric materials. This is a continuum damage model based on the Matzenmiller-Lubliner-Taylor theory [40] intended to describe the failure of woven fabrics and composite laminates, also accounting for post-critical behaviour. More details about the model are reported in the Supplementary Information, Section 2.2 and the input parameters for carbon, glass, and PA fibres, as extracted from our experiments, and for the epoxy resin (as specified by the producer) are reported in Supplementary Tables S5-S8. Average values of thickness and volume fraction reported in Table 1 were used. Thus, in total 18 simulations were performed corresponding to single cases determined by material, number of layers, and orientation of the textile with respect to the application of the load.

2.3. FEM impact simulations

Four armours, based on the characterized materials and corresponding to the conducted experimental test, were simulated: a 17-layer carbon-based armour with overall thickness of 4 mm ($f = 0.510$), a 16-layer glass-based armour with a thickness of 3 mm ($f = 0.640$), and two 30-layer PA armours with thicknesses of 5 and 7 mm ($f = 0.599$ and $f = 0.429$, respectively). The integration scheme, element formulation, and

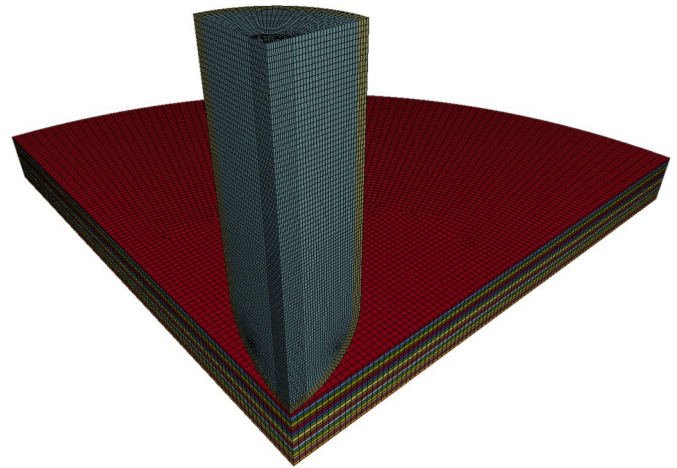


Fig. 2. Finite element model for impact simulation (Carbon T800 17-layer laminate).

material model follow the same setup adopted for the tensile testing simulations. The integration scheme for the four tested armours is reported in detail in Table S4 in the Supplementary Information. The simulated target is comprised of a circular plate (only one quarter is simulated due to the symmetry of the system) subjected to the impact of a lead/copper projectile simulating a FMJ Remington 9 mm Parabellum (radius $r = 4.51$ mm and mass $m_p = 8.04$ g) traveling at 360 m/s (Fig. 2), i.e. resulting in an impact energy of about 520 J. The plate radius is $R = 40$ mm, which is about 9 times larger than the radius of the projectile, so that edge effects can be neglected, and the plate is fully clamped at the external edge. The woven orientation from each layer to the next progressively increases by an angle of 45° (i.e. stacking sequence: $k [0^\circ, 45^\circ, 90^\circ, -45^\circ]$). One single element through the thickness was used to model the single plies. Given the variable thickness of the plies of the various targets, the aspect ratios for the elements in the region under impact ($< 3r$) are in the range $\sim 1:1:0.42$ (x, y, z) to $\sim 1:1:0.59$, with an in plane characteristic size of about 0.40 mm (see detail of the mesh in Figure S4 in the Supplementary Information) as results from the performed convergence study (see Section S2.1, Figure S3 in the Supplementary Information).

An eroding type segment-to-segment contact is implemented between the layers (static and dynamic coefficient of friction equal to $\mu_s = 0.20$, $\mu_d = 0.15$, respectively [41]). A stress-based segment-to-segment tiebreak type contact (LS-DYNA - Option 6) is implemented to model inter-layer adhesion and delamination with normal and shear limit stresses equal to NFLS = 0.35 GPa and SFLS = 0.10 GPa, respectively. Finally, a segment-to-segment contact is implemented between the projectile and the target layers ($\mu_s = 0.40$, $\mu_d = 0.30$ [41]): in this case the SOFT = 2 option is activated to prevent interpenetration, given the high mismatch between the projectile and the composite contact stiffnesses. No scaling of the contact stiffness of the slave/master surfaces is implemented in the contact. More details of the contact implementation can be found in the Supplementary Information, Section 2.4 where the script lines regarding contact implementation are also reported (Tables S9-S11). Failure within the armour is implemented by means of element erosion, which is based on the failure criterion of the specific material model (MAT_58 [40]): when failure is reached at all the integration points the element is deleted from the simulation, properly accounting for its energy in the overall balance. Again, hourglass energy is verified to be less than 5% of the deformation energy at each simulation timestep for the whole model and for each of its deformable parts separately. The total simulation time for all simulations is 0.07 ms, ensuring complete stop or penetration of the target with stabilization of the projectile residual velocity (V_{res}).

In this work, strain-rate effects on material properties, although

Table 2
Average tensile mechanical and volumetric properties of the single fibres.

	Carbon	E-Glass	PA
Young's modulus [GPa]	232.77 ± 19.6	55.11 ± 20.2	95.27 ± 9.7
Fracture strength [GPa]	4.12 ± 0.7	1.24 ± 0.4	2.82 ± 0.4
Ultimate strain	0.018 ± 0.004	0.023 ± 0.007	0.030 ± 0.001
Toughness (av.) [J/m ³]	0.0365	0.0140	0.0417
Diameter [μm]	6	20	12
Density [kg/m ³]	1810	2540	1445
U ^{1/3} (av.) [m/s]	611	300	617

generally important for these problems, are not considered, for two reasons. Firstly, while the absolute magnitude of material properties could be affected, their size-scaling would be negligible. Secondly, the analysis of interest in this work for the impact behaviour through the dimensionless Cuniff parameter ($V_{50}/U^{1/3}$) conceptually eliminates the strain-rate dependency of results.

3. Results and discussion

3.1. Characterization of single fibres and fibre bundles

Typical results for mechanical microtensile tests and fibre volumetric characterization are summarized in Table 2. The fibres display approximately a linear stress-strain behaviour up to failure, which occurs between 1% and 3.1% strain, and between 1.24 and 4.17 GPa stress, with glass fibres displaying a considerably smaller strength, carbon displaying the maximum strength and PA the maximum toughness (integral of the force-displacement curve divided by the fibre mass). The results fall within the reported range in existing literature [3,33,42]. PA also displays the largest Cuniff parameter, and is thus expected to be the most suitable material for energy dissipation by material failure.

Typical stress-strain results for various fibre bundle samples are shown in Fig. 3, and the extracted mechanical parameters reported in Table 3. In general, tests on fibre bundles yield smaller strength values compared to single fibres (Fig. 4). This can be attributed to the statistical distributions in the strength and in the ultimate strain of the single fibres, leading to a non-simultaneous breaking of the fibres (Fig. 3), as predicted by HFBM [19,20]. This is demonstrated by the various peaks in the stress-strain curves, and a maximum stress reached for a given percentage of surviving fibres (Fig. 3). This type of mechanical test

provides a more reliable estimation of the properties of the fibre yarns in the composites, and thus we used these values in the numerical simulations. Using classical Weibull's statistic [43] to study the distribution of the fracture strength of bundles under uniaxial uniform stress, we have:

$$F(\sigma_{f,i}) = 1 - \exp \left[- \frac{A_i}{A_0} \left(\frac{\sigma_{f,i}}{\sigma_{A,0}} \right)^{1/m} \right] \quad (1)$$

where $\sigma_{A,0}$ and m are the Weibull's shape and scale parameters, respectively, for a specific set of samples (material) and $F(\sigma_{f,i}) = (i - \frac{1}{2})/N$ is the probability of failure of the N samples sorted in order of increasing strength [44] (data in Table S12 in the Supplementary Information). A_0 and $\sigma_{A,0}$ are in our case the average values of the cross-section area and of the tensile strength, respectively, of the single fibre of the considered material (determined from diameter and strength values, respectively, reported in Table 2). For the studied materials we determine m to be 9.4, 29.9, 26.8 for carbon, E-glass, and PA fibres, respectively. The quasi-linear behaviour up to fracture in PA bundle stress-strain curves implies that there is small dispersion on the strength values of the single fibres, contrary to the carbon and E-glass cases (Fig. 3), as also quantified by the Weibull analysis. Carbon fibres display high strength values but fragile fracture and dispersion in strength values, which may lead to low fracture toughness, and therefore limited impact strength. PA fibres, on the other hand, exhibit good strength characteristics with greater toughness values. Finally, E-Glass yarns have smaller strength values as compared to carbon and PA.

Table 3

Average tensile mechanical and volumetric properties of the fibre bundles. Values for all tested samples for Weibull analysis are reported in Table S12 in the Supplementary Information.

	Carbon	E-Glass	PA
Young's modulus [GPa]	85.7 ± 10.13	48.32 ± 8.68	72.94 ± 4.14
Fracture strength [GPa]	2.17 ± 0.27	0.995 ± 0.04	2.52 ± 0.09
Strain at peak stress	0.026 ± 0.003	0.021 ± 0.001	0.031 ± 0.001
Ultimate strain	0.031 ± 0.004	0.027 ± 0.002	0.031 ± 0.001
Area [mm ²]	0.255 (0.246 ^a)	0.113 (0.118 ^a)	0.092 (0.084 ^a)
Weibull parameter m	9.4	29.9	26.8

^a Value obtained as ratio of the linear density of the textile in [dtex], as declared by the producers, and the volumetric bulk density of the material in [kg/m³], is included for validation of performed measure.

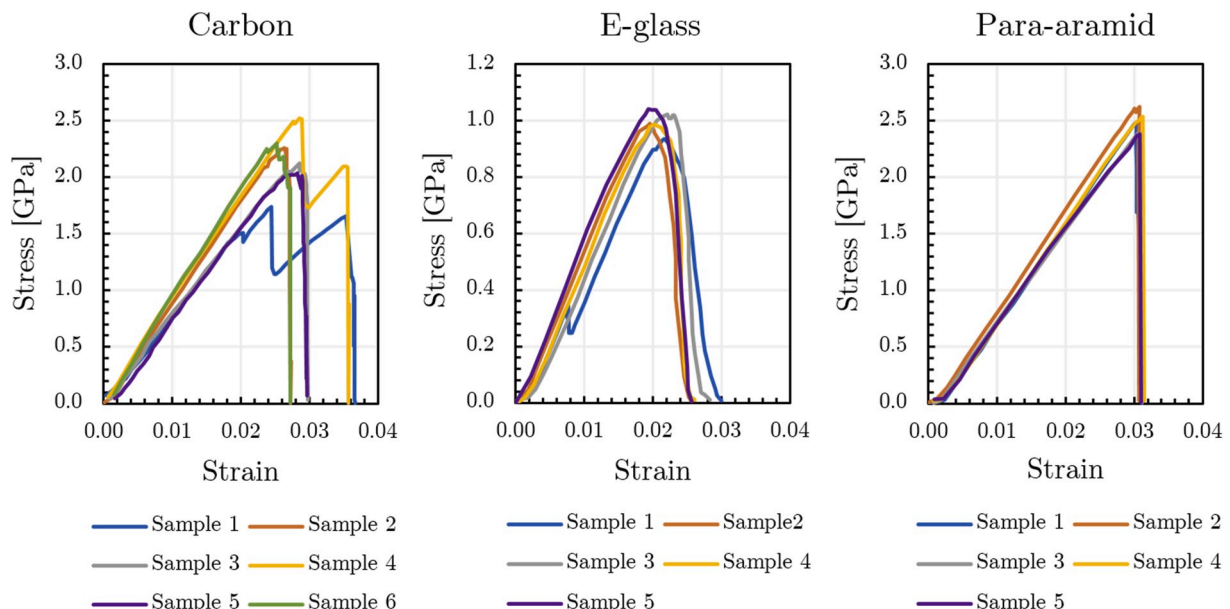


Fig. 3. Experimental tensile stress-strain curves for various samples of carbon, E-glass and PA fibre bundles tested up to failure.

Table 4

Average laminate tensile strength (and related standard deviation) from experimental data and comparison with FEM simulation results (values extracted from Fig. 6 and Figures S5-S12 in the Supplementary Information) and prediction from rule of mixture (Equation (2)).

	1 layer			5 layers			10 layers		
	Exp.	FEM	Eq. 2	Exp.	FEM	Eq. 2	Exp.	FEM	Eq. 2
Carbon	367.61 ± 99.10	498.00	979.41	533.16 ± 42.44	485.56	1065.29	515.40 ± 60.78	473.10	1004.61
E-glass	208.19 ± 6.15	249.00	474.93	329.75 ± 48.93	348.61	670.81	308.87 ± 11.55	344.18	696.10
PA	542.18 ± 79.80	498.02	1377.74	460.25 ± 34.09	560.26	1660.00	308.40 ± 16.14	401.38	1191.25

	1 layer			5 layers			10 layers		
	Exp.	FEM	Eq. 2	Exp.	FEM	Eq. 2	Exp.	FEM	Eq. 2
Carbon	76.30 ± 10.40	122.60	480.78	107.60 ± 11.30	110.71	546.08	79.87 ± 20.51	99.64	589.42
E-glass	50.01 ± 27.69	77.50	229.30	50.68 ± 11.55	66.43	284.90	54.80 ± 13.59	71.96	354.59
PA	66.67 ± 18.81	66.42	547.38	49.34 ± 5.88	66.92	886.72	32.93 ± 13.90	42.31	660.03

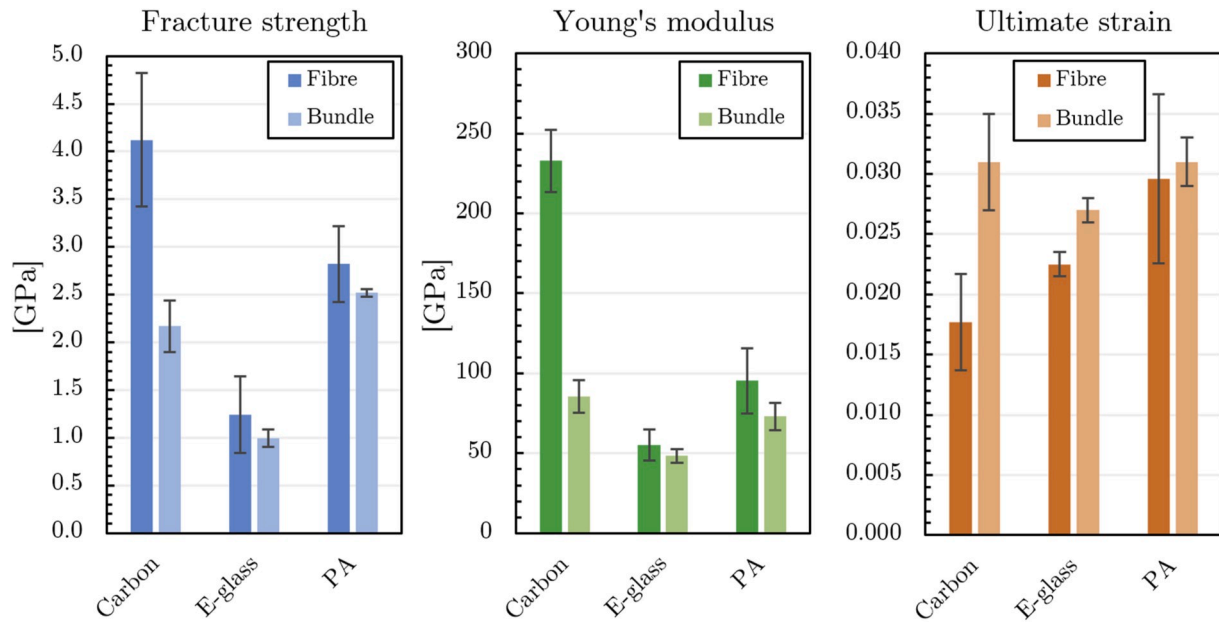


Fig. 4. Comparison of average strength, Young's modulus, and ultimate strain (and related standard deviations) for Carbon, E-glass and PA fibres and corresponding bundles.

Our Weibull's analysis is qualitatively and quantitatively in agreement with other results of systematic studies recently published [42], showing the consistent measurement of properties at the fibre and bundle scale.

3.2. Scaling of laminate properties

Results for uniaxial tests on dog-bone specimens for 1-ply, 5-ply and 10-ply laminates are summarized in Fig. 5. These results are compatible with those commonly found in literature for the considered materials [45,46]. As an example case, the resulting experimental stress-strain curves for 1-ply PA laminates (0° and 45° woven direction), together with the results of the numerical simulations, are reported in Fig. 6 (for the experimental and simulation-derived stress-strain curves of all other materials and laminates with different number of plies see Figures S5-S12 in the Supplementary Information).

In Fig. 5 we can observe from simulation values that, generally, the strength decreases with the increase of the number of layers according to well-known size effects on fracture properties. This trend is occasionally inverted due to the fact that the tested experimental samples, and thus the simulated counterparts, are not compared over an equal volume fraction basis, originated by the production process. Indeed, a clear dependence of strength on the volume fraction is observed (especially in

PA and E-glass laminates in Fig. 5). Simulation and experiment are generally in good agreement, although a significant variability in the experimental results is observed, especially in the 1-ply Carbon based samples, probably due to residual defects from manufacturing. This underlines the importance of the production process in providing final composite with actual predicted mechanical properties from its constituents and a sufficient and reliable level of performance, as well as the employment of reliable simulation models when few characterization tests are available. The in-plane fracture strength of the composite laminates ($\sigma_c = \max\{\sigma\}$), with different orientation θ of the woven with respect to the direction of application of the load, can be derived from the fracture strength of the fibres (σ_f) and matrix (σ_m) by application of the following rule of mixture which takes in to account the orthotropic nature of the woven textile:

$$\begin{Bmatrix} \sigma_{c,x} \\ \sigma_{c,y} \end{Bmatrix} = f \begin{Bmatrix} \sigma_{f,1} \\ \sigma_{f,2} \end{Bmatrix} \begin{bmatrix} \cos^4\theta & \sin^4\theta \\ \sin^4(\theta + \frac{\pi}{2}) & \cos^4(\theta + \frac{\pi}{2}) \end{bmatrix} + (1-f) \begin{Bmatrix} \sigma_{m,1} \\ \sigma_{m,2} \end{Bmatrix} \quad (2)$$

where the subscript x,y represents the loading direction of the composite, the subscripts 1 and 2 indicate the mutually orthogonal directions of the warp and weft of the woven textile (see Figure S2 in the

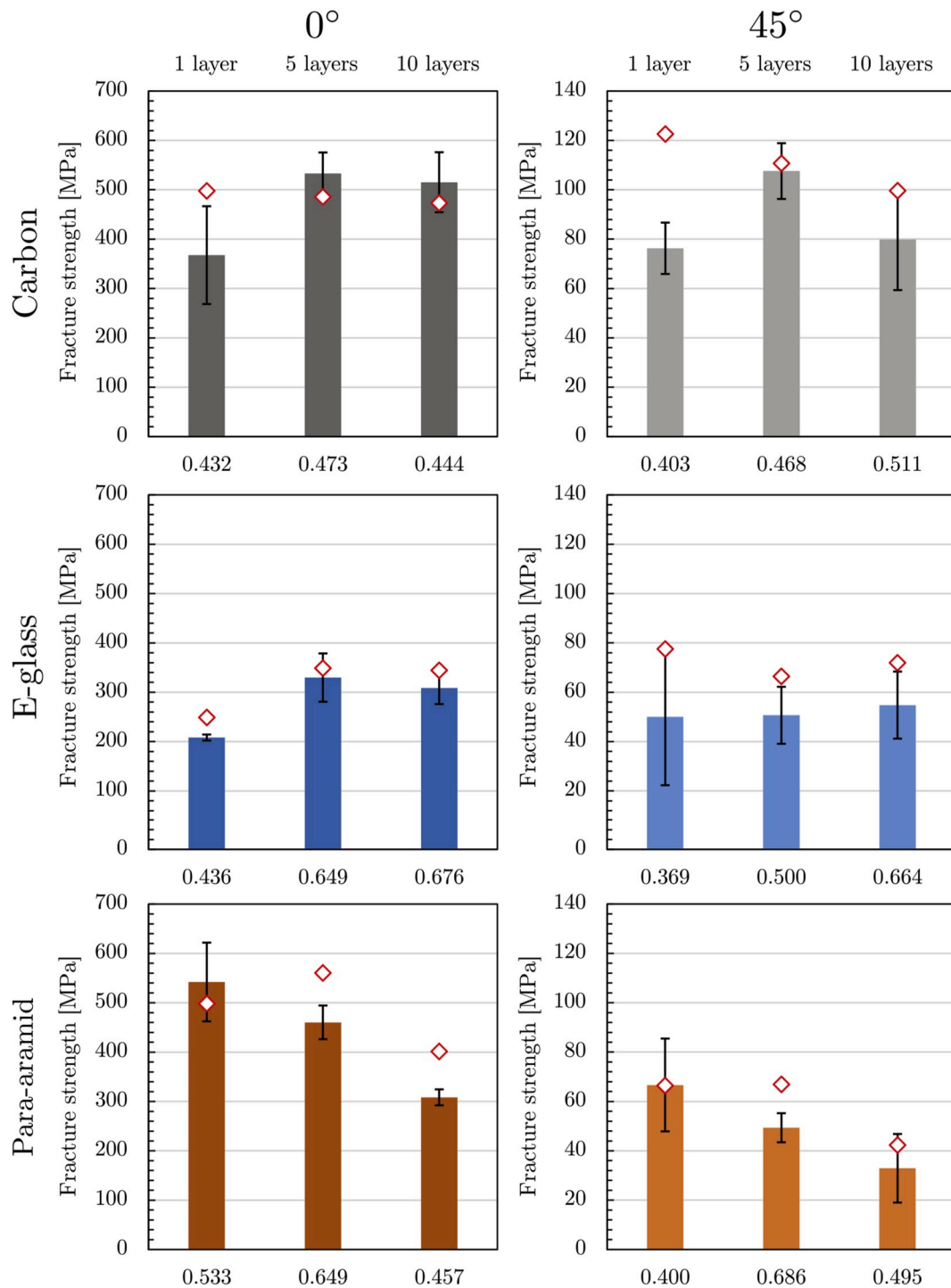


Fig. 5. Laminate tensile strength from experimental data (columns representing mean, standard deviation is reproduced by bars) and comparison with FEM simulation results (red dots). See Table 4 for the corresponding numerical values. (For interpretation of the references to colour in this figure legend, the reader is referred to the Web version of this article.)

Supplementary Information for the notation of quantities). Note that corresponding mechanical properties for both fibre (bi-directional textiles) and matrix (isotropic material) are equal in our case (i.e., $\sigma_1 = \sigma_2$) and that we have assumed for the woven reinforcement material $\sigma_{12} = 0$, i.e. to be negligible with respect to the corresponding counterparts in the principal direction. Results from Equation (2) (fracture strength $\sigma_{c,x} = \sigma_{c,y}$) are reported in Table 4. It is evident how the rule of mixtures significantly overestimates the properties of the composite for both orientations of the laminae with respect to the applied load.

Alternatively, by back calculating the textile strength using Equation (2), we obtain significantly smaller values than those actually measured for the single bundle, showing, as expected, size-scale effects on material properties (Figure S13 in the Supplementary Information). Thus, experiments and simulations are necessary complementary tools to characterize the material at the laminate level and predict accurate values of the fracture strength.

Analysing the stress-strain curves reported in Fig. 6 (and Figures S5-S12 in the Supplementary Information) we observe that under tensile

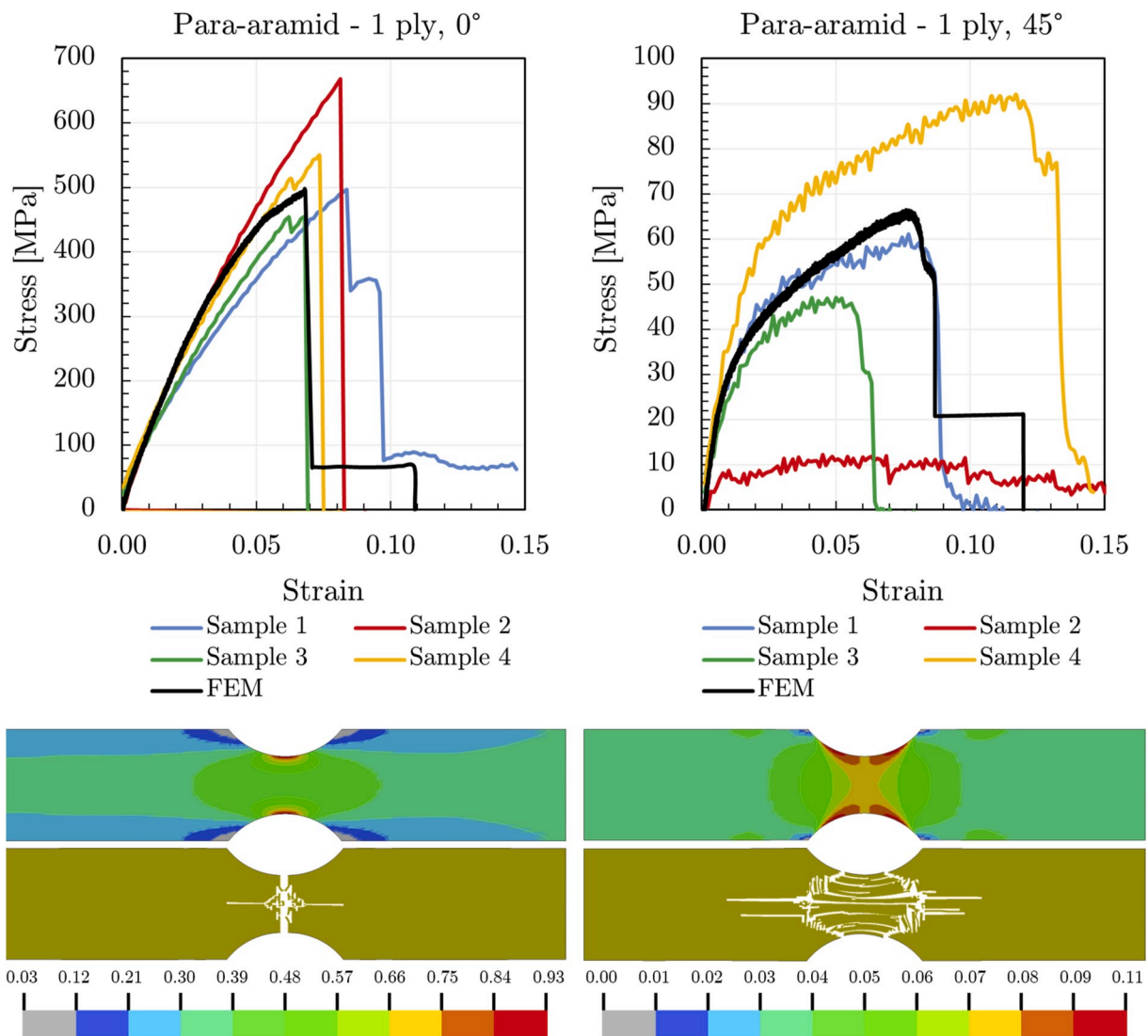


Fig. 6. Experimental and FEM stress-strain curves for 1 ply of PA laminate at 0° (left panels) and 45° (right panels) of orientation of the warp with respect to the direction of application of the load (horizontal direction, see [Figure S2](#) in the Supplementary Information). Fibre volume fractions are 0.533 and 0.400 respectively. The bottom panel shows, for the two orientations, the contour plot of von-Mises stress (in GPa) at the failure onset and the images of the failed samples (eroded elements) as obtained from FEM simulations.

load, in general, a first sublinear phase is present, during which there is simultaneous matrix fracture, fibre debonding and fracture in the loading direction, up to the maximum load [4]. This progressive failure and softening is also predicted by FEM where all these mechanisms cannot be accounted for, but this behaviour derives from the delayed reaching of the post peak phase and overcoming of the failure criterion at each integration points through the thickness of the thick shell elements. Subsequently, there is an unloading phase with residual effects due to frictional sliding of the reinforcing fibres in the matrix and residual matrix strength up to final fracture.

It can be noticed that when loading is applied at a 45° angle with respect to the fibre direction (θ), there is a greater variability in the results for stress/strain curves: this is due to the greater sensitivity with respect to geometrical (i.e., fabrication) imperfections and the consequent variability in determining the onset and propagation of damage, i. e. the post-peak stress-strain behaviour. In this case, experimental curves have a common initial slope (i.e. Young's modulus), but vary considerably in the damage evolution part of the curve. Despite this, the FEM simulations correctly reproduce the average experimental behaviour, in terms of average fracture strength, ultimate strain, and specific toughness values.

3.3. FEM impact simulations

[Fig. 7](#) reports the results of FEM impact simulations, in terms of evolution of the projectile translational velocity vs. time for the four armours analysed under ballistic tests. The projectile residual velocities after impact (V_{res}) predicted by FEM simulations are 103 m/s, 115 m/s, 0 m/s (stopped projectile), and 3 m/s for tests on carbon, E-glass, PA ($t = 5$ mm, and $t = 7$ mm, respectively). The corresponding experimental values [47] are 110 m/s, 110 m/s, 27 m/s, and 0 m/s, respectively. Note that in the case of PA armor, where the projectile impact velocity is near the critical limit V_{50} , the difference in the occurrence of perforation between experiments and simulations falls within the statistical variation and model uncertainty. [Fig. 8](#) provides a visual comparison between the damage distribution in simulated plates and experiments, showing good agreement in the deformation behaviour. Thus, the developed numerical model, based on the mechanical properties of each single component, is able to predict with a good level of reliability the energy absorption capability of the targets, related damage and failure mechanisms. It is also verified that in the velocity regime analysed in this work, strain-rate effects are negligible even in absolute terms (see [Figure S14](#) in the Supplementary Information).

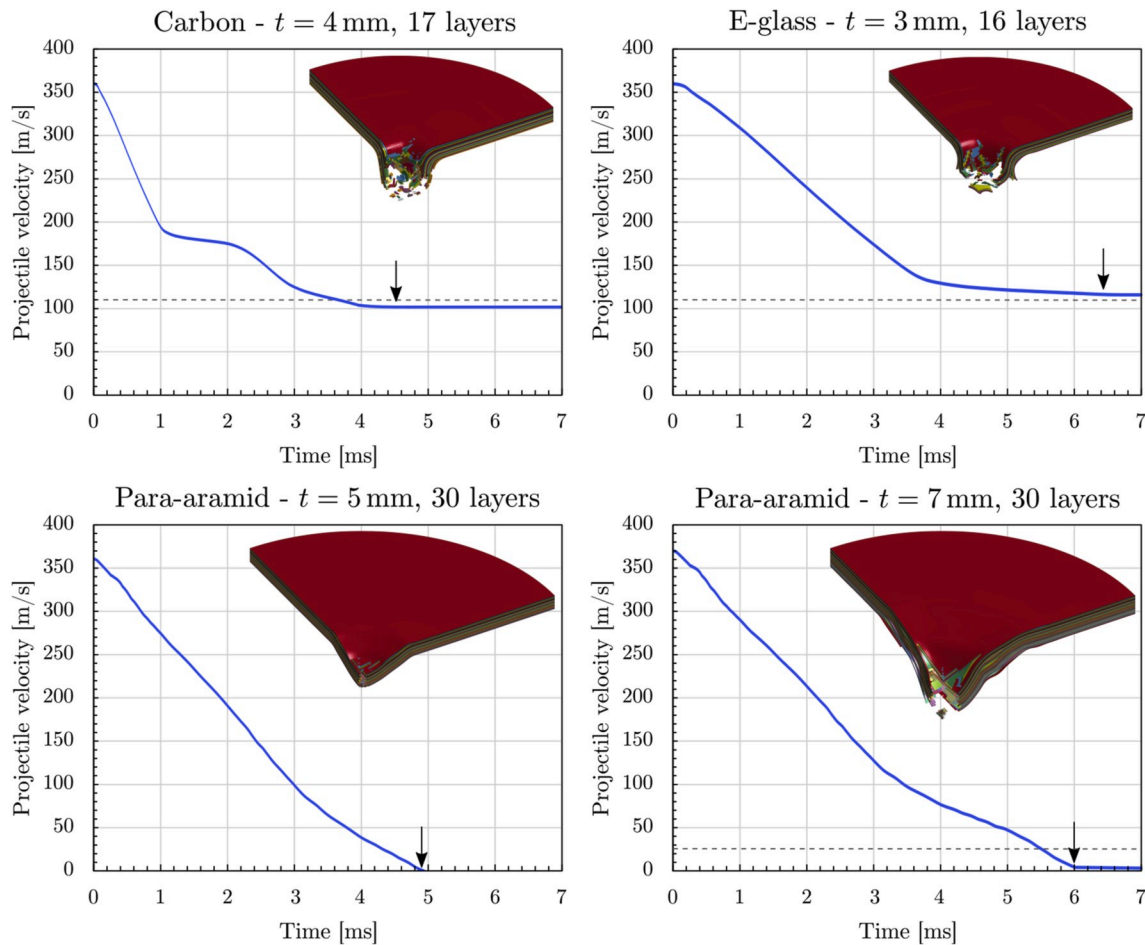


Fig. 7. Evolution of the projectile velocity over time after impact with the four tested targets by FEM simulation. The dashed lines represent the reference value of the residual velocity determined from ballistic experiments [47] (for the PA plate with $t = 5$ mm both simulation and experiment provide $V_{res} = 0$). The insets depict the snapshots of FEM simulations taken at the time at which the projectile velocity stabilizes after the strike, either with $V_{res} > 0$ or with stopping of the projectile, highlighted by the arrows on the curves.

As expected, high strength fibres with limited toughness due to low ultimate strain (carbon) or low strength (glass) display a more localized damage and, consequently, their absolute and specific impact toughness is smaller with respect to PA plates. On the contrary, PA plates are able to undergo larger and less localized deflection and deformation, also promoting delamination over a wider area, giving a more synergistic contribution of energy dissipation between the layers [12]. This translates overall into higher impact energy absorption capability. However, a primary requirement in ballistic applications, especially for body armours, is to minimize the target perforation depth and deformation: in this sense, a good balance between fracture strength and ultimate strain to failure is necessary to maximize the toughness –or to avoid its impairment– within given deformability constraints. Our results are in agreement with observation at lower impact velocities [33,34].

From the comparison of the two PA plates, it is possible to notice the effect of the composite volume fraction, derived from different curing pressures and temperatures, which allows the thinner 5 mm plate to stop the projectile in a shorter time (and thickness) providing a higher specific energy absorption capability (energy per layer or per areal density) with respect to the 7 mm thickness counterpart. This aspect is not predicted by the classical dimensional analysis [11]. To rationalize this latter result and evaluate and compare the energy absorption capability of the three materials when used as reinforcement in armours, we propose a multiscale generalization to heterogeneous materials of the Cuniff parameter, originally developed for plain textiles, by taking into account the composite nature of the target, as follows:

$$U_m \sim \frac{[f\sigma_t + (1-f)\sigma_m]^2}{2[f\rho_{bundle} + (1-f)\rho_m][fE_{bundle} + (1-f)E_m]} \sqrt{\frac{E_{bundle}}{\rho_{bundle}}} \quad (3)$$

where the properties of the bundle, which can be in turn inferred by the properties of the single fibres through Equation (1), are explicitly considered. Note that the composite material strain is here calculated as $\varepsilon_c = \frac{\sigma_c}{E_c} = \frac{[f\sigma_t + (1-f)\sigma_m]}{[fE_{bundle} + (1-f)E_m]}$, while the term under the square root related to the dissipation by elastic waves accounts only for the reinforcement phase since the elastic wave will be guided in the plane primarily within the stiffer phase of the composite, i.e. the textile, regardless of the fibre volume fraction f .

Results scaled according to Equation (3) are reported in Fig. 9, allowing to compare on the same graph the performance of different reinforcing materials also structured in the composite in different ways (volume fraction and number of layers). It is then possible to make a more realistic comparison among materials, for example taking into account the issues that some textile or mould geometries may create in obtaining desired volume fraction, due to specific difficulties in the production process [48]. The good correlation between the lower scale material parameters (input) derived experimentally and the performance of the armour extracted from ballistic impact simulations (output) shows the good capability of the modified criterion, as well as the inferring of properties from single constituents, to predict the impact performance at the macro-scale, starting from the properties of the constituents at the micro-scale and their arrangement at the meso-scale.

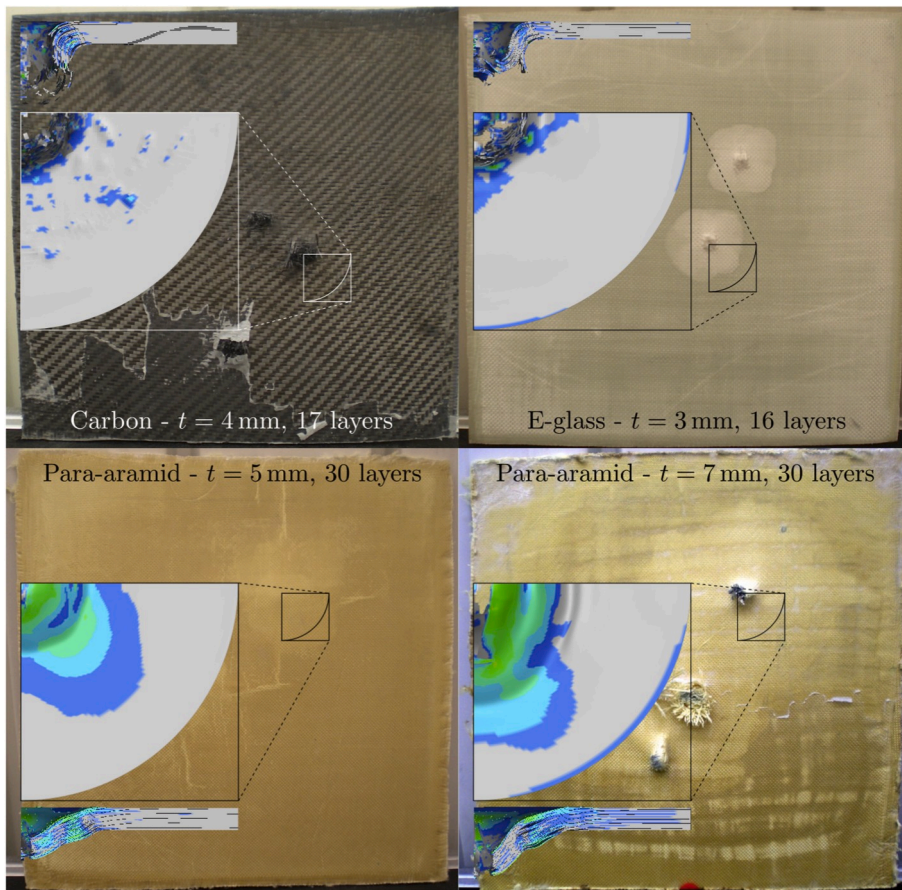


Fig. 8. Visual comparison after impact at $V_{res} = 360$ m/s between experimental (rear face) and simulated targets (rear face and cross section). The magnified regions have a size of 40×40 mm² (overall size of the experimental target is $\sim 370 \times 370$ mm²) and refer to the first impact performed on the armour. The stresses in the FEM images (von-Mises) are plotted to highlight qualitatively the radius of the zone affected by the impact and compare it with the deformation observed in experiments. Experimental pictures courtesy of Vemar Helmets s.r.l..

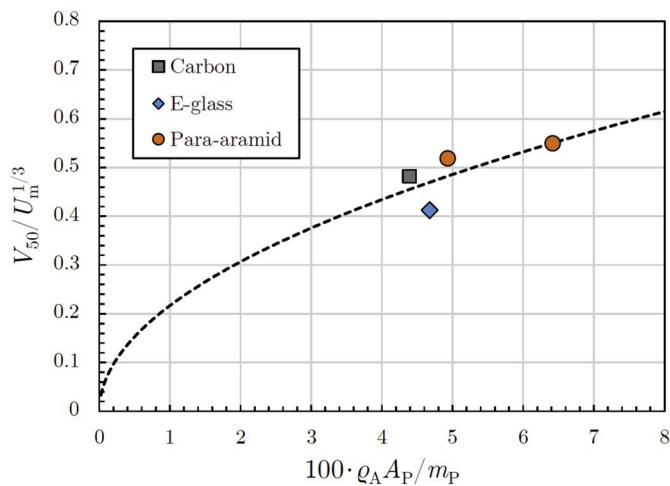


Fig. 9. Comparison on the Cuniff map of the three tested materials and four armours structures by Equation (3). The ballistic limit velocity V_{50} is extracted from FEM simulations and corresponds, in this case, to the condition $V_{res} = 0$. ρ_A is the areal density of the target while $A_P = \pi r^2$ is the projected area of the projectile with mass m_P (same for all cases).

Thus, the proposed multiscale characterization process, summarized in Fig. 10, can provide a preliminary and effective assessment of the suitability of different reinforcing materials and the selection of optimal ones for impact energy absorption and shielding.

4. Conclusions

In this paper, we have proposed a multiscale coupled experimental/numerical framework to provide consistent and reliable correlation between tensile (quasi-static) and impact properties of composite laminates. Starting from the characterization of the single fibres using a nanotensile testing machine and of fibre bundles at mesoscale, we used the measured tensile properties as input for a non-linear FEM model to predict the tensile fracture properties of the laminates at macroscale, verifying them with experimental results. Then, a multilayer integration model for single plies was assembled and employed to construct, via the introduction of contact algorithms and proper boundary conditions, a numerical model of multilayer armours subjected to high-velocity impact, whose predictions were verified with ballistic tests. The predictions of impact energy absorption obtained by using microscale properties are in good agreement with experimental results, additionally showing a direct correlation between the fibre properties and their structural arrangement (in terms of volume fraction) with the limit ballistic velocity, by employing a proposed multiscale generalization of the Cuniff parameter. We have thus demonstrated that a characterization of the mechanical properties via simple tensile tests can help to preliminarily assess and compare the suitability of different materials for employment as reinforcement in composite armours for ballistic application. The multiscale characterization presented in this work can allow to extend traditional design concepts of composites for ballistic applications to novel nanofibres and nanocomposites [49,50], with the potential capability to also integrate the role of hierarchical structures and geometries at multiple levels.

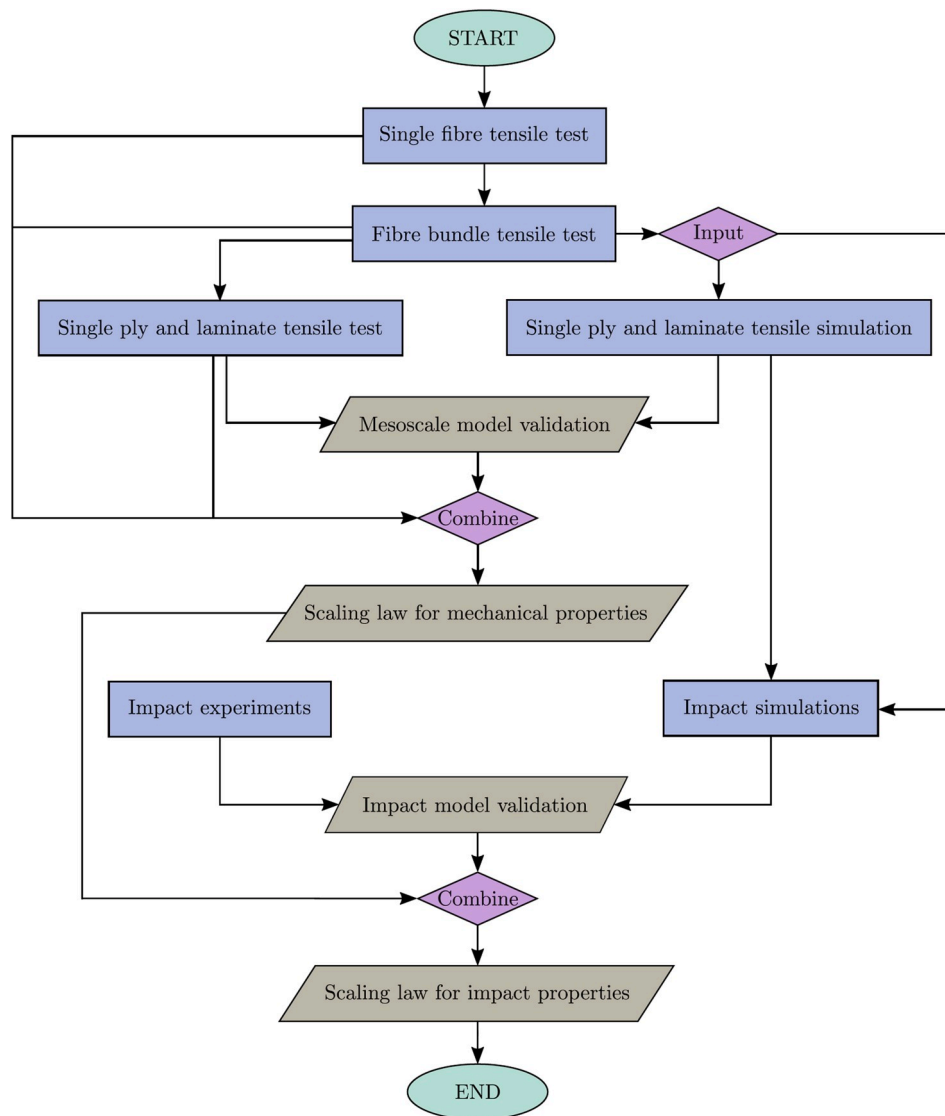


Fig. 10. Flow chart of the proposed experimental/numerical approach for the scaling assessment of material properties for impact studies.

CRediT authorship contribution statement

Stefano Signetti: Methodology, Software, Validation, Formal analysis, Investigation, Writing - original draft, Writing - review & editing, Visualization. **Federico Bosia:** Conceptualization, Methodology, Validation, Formal analysis, Investigation, Writing - original draft, Writing - review & editing. **Seunghwa Ryu:** Formal analysis, Writing - review & editing. **Nicola M. Pugno:** Conceptualization, Methodology, Formal analysis, Writing - review & editing, Supervision, Funding acquisition.

Acknowledgements

NMP is supported by the European Commission under the Graphene Flagship Core 2 grant No. 785219 (WP14 “Composites”), FET Proactive “Neurofibres” grant No. 732344, FET Open “Boheme” grant No. 863179 as well as by the Italian Ministry of Education, University and Research (MIUR) under the “Departments of Excellence” grant L. 232/2016, the ARS01-01384-PROSCAN and the PRIN-20177TTP3S grants. FB is supported by H2020 FET Proactive Neurofibres Grant No. 732344, by project Metapp (n. CSTO160004) co-funded by Fondazione San Paolo, and by the Italian Ministry of Education, University and Research (MIUR) under the “Departments of Excellence” grant L. 232/2016. SHR is supported by the Basic Science Research Program

(2019R1A2C4070690) and the Creative Materials Discovery Program (2016M3D1A1900038) through the National Research Foundation of Korea (NRF). SS acknowledges financial support from Brain Korea 21 Plus Postdoc Scholarship (NRF) and Ermenegildo Zegna Founder’s Scholarship 2017–2018.

Appendix A. Supplementary data

Supplementary data to this article can be found online at <https://doi.org/10.1016/j.compositesb.2020.108090>.

References

- [1] LaSalvia JC, Gyekenyesi A, Halbig M, editors. *Advances in ceramic armors X. Of ceramic engineering and science proceedings*, vol. 35. Wiley; 2014.
- [2] Signetti S, Nicotra M, Colonna M, Pugno NM. Modeling and simulation of the impact behavior of soft polymeric-foam-based back protectors for winter sports. *J Sci Med Sport* 2019;22(S1):S65–70.
- [3] Tenney DR, Davis JG, Pipes RB, Johnston N. *NASA composites material development: lesson Learned and future challenges*. NATO RTO AVT-164 workshop on support of composite systems, bonn, Germany. 2009.
- [4] Hoog PJ. Composites in armor. *Science* 2006;314(5802):1100–1.
- [5] Cantwell WJ, Morton J. The impact resistance of composite materials - a review. *Composites* 1991;22(5):347–62.

- [6] Kumar BG, Singh RP, Nakamura T. Degradation of carbon fibre-reinforced epoxy composites by ultraviolet radiation and condensation. *J Compos Mater* 2002;36(24):2713–33.
- [7] Harris B. *Engineering composite materials*. second ed. London, UK: Institute of Materials; 1999.
- [8] Ganczakowski H, Beaumont PWR. The behaviour of Kevlar fibre-epoxy laminates under static and fatigue loading. Part 1: Experimental. *Compos Sci Technol* 1989;36:299–319.
- [9] Cheeseman BA, Bogetti TA. Ballistic impact into fabric and compliant composite laminates. *Compos Struct* 2003;61(1–2):161–73.
- [10] Leong KH, Lee B, Herszberg I, Bannister MK. The effect of binder path on the tensile properties and failure of multilayer woven CFRP composites. *Compos Sci Technol* 2000;60(1):149–56.
- [11] Cuniff PM. Dimensionless parameters for optimization of textile-based body armor systems. Proceedings of the 18th international symposium of ballistics. San Antonio, TX, USA. 1999. p. 1303–10.
- [12] Signetti S, Pugno NM. Evidence of optimal interfaces in bio-inspired ceramic-composite panels for superior ballistic protection. *J Eur Ceram Soc* 2014;34(11):2823–31.
- [13] Iremonger MJ, Went AC. Ballistic impact of fibre composite armours by fragment simulating projectiles. *Compos. Part A-App S* 1996;27(7):575–81.
- [14] Cantwell WJ. PhD thesis. In: Impact damage in carbon fibre composites. London: Imperial College; 1986.
- [15] Baucom JN, Zikry MA. Evolution of failure mechanisms in 2D and 3D woven composite systems under quasi-static perforation. *J Compos Mater* 2003;37(18):1651–74.
- [16] Cox BN, Flanagan G. *Handbook of analytical methods for textile composites*. Hampton, VA, USA: National Aeronautics and Space Administration (NASA), Langley Research Center; 1997. Technical report.
- [17] Hosur MV, Vaidya UK, Ulven C, Jeelani S. Performance of stitched/unstitched woven carbon/epoxy composites under high velocity impact loading. *Compos Struct* 2004;64(3–4):455–66.
- [18] Ulven C, Vaidya UK, Hosur MV. Effect of projectile shape during ballistic perforation of VARTM carbon/epoxy composite panels. *Compos Struct* 2003;61(1–2):143–50.
- [19] Pradhan S, Hansen A, Chakrabarti BK. Failure processes in elastic fiber bundles. *Rev Mod Phys* 2010;82(1):499–555.
- [20] Pugno NM, Bosia F, Abdalrahman. Hierarchical fiber bundle model to investigate the complex architectures of biological materials. *Phys Rev E* 2012;85(1):011903.
- [21] Bosia F, Abdalrahman T, Pugno NM. Investigating the role of hierarchy on the strength of composite materials: evidence of a crucial synergy between hierarchy and material mixing. *Nanoscale* 2012;4(4):1200–7.
- [22] Reissner E. The effect of transverse shear deformation on the bending of elastic plates. *J Appl Mech* 1945;12:69–76.
- [23] Mindlin RD. Influence of rotary inertia and shear in flexural rotations of isotropic elastic plates. *J Appl Mech* 1951;18(1):31–8.
- [24] Reddy JN. An evaluation of equivalent-single-layer and layerwise theories of composite laminates. *Compos Struct* 1993;25(1–4):21–35.
- [25] Caliri Jr MF, Ferreira AJM, Tita V. A review on plate and shell theories for laminated and sandwich structures highlighting the Finite Element Method. *Compos Struct* 2016;156:63–77.
- [26] Abrate S, di Sciuva M. Equivalent single layer theories for composite and sandwich structures: a review. *Compos Struct* 2017;179:482–94.
- [27] Epstein M, Glockner PG. Nonlinear analysis of multilayered shells. *Int J Solid Struct* 1977;13(11):1081–9.
- [28] Reddy JN. On the generalization of displacement based laminate theories. *Appl Mech Rev* 1989;42:213–22.
- [29] Lim CT, Shim VPW, Ng YH. Finite-element modeling of the ballistic impact of fabric armor. *Int J Impact Eng* 2003;28(1):13–31.
- [30] Gama BA, Gillespie JW. Finite element modeling of impact, damage evolution and perforation of thick section composites. *Int J Impact Eng* 2011;38(4):181–97.
- [31] Signetti S, Taioli S, Pugno NM. 2D material armors showing superior impact strength of few layers. *ACS Appl Mater Interfaces* 2017;9(46):40820–30.
- [32] Chen C-T, Gu GX. Machine learning for composite materials. *MRS Commun* 2019;9(2):556–66.
- [33] Claus J, Santos RAM, Gorbatikh L, Swolfs Y. Effect of matrix and fibre type on the impact resistance of woven composites. *Compos. Part B-Eng.* 2020;183:107736.
- [34] Xu ZW, Chen YH, Cantwell WJ, Guan ZW. Multiscale modeling of scaling effects in the impact response of plain woven composites. *Compos. Part B-Eng.* 2020;183:107885.
- [35] ASTM C1557-20. Standard test method for strength and Young's modulus of fibres. West Conshohocken, PA, USA: ASTM International; 2020.
- [36] ASTM D3039/D3039M-17. Standard test method for tensile properties of polymer matrix composite materials. West Conshohocken, PA, USA: ASTM International; 2017.
- [37] Hallquist J. *LS-DYNA theory manual*. CA, USA: Livermore Software Technology Corporation; 2006.
- [38] Liu WK, Guo Y, Tang S, Belytschko T. A multiple-quadrature eight-node hexaedral finite element for large deformation elastoplastic analysis. *Comput Methods Appl Mech Eng* 1998;154(1–2):69–132.
- [39] Belytschko T, Ong JSJ, Liu WK, Kennedy JM. Hourglass control in linear and nonlinear problems. *Comput Methods Appl Mech Eng* 1984;43(3):251–76.
- [40] Matzenmiller A, Lubliner J, Taylor RL. A constitutive model for anisotropic damage in fibre composites. *Mech Mater* 1995;20(2):125–52.
- [41] Lopes G, Gürdal Z, Camanho PP, Maimí P, González EV. Simulation of low velocity impact damage on composite laminates. 50th AIAA/ASME/ASCE/AHS/ASC structures, structural dynamics, and materials conference. Palm springs, CA, USA. 2009.
- [42] Naresh K, Shankar K, Velmurugan R. Reliability analysis of tensile strengths using Weibull distribution in glass/epoxy and carbon/epoxy composites. *Compos. Part B-Eng.* 2018;133:129–44.
- [43] Weibull W. A statistical distribution function of wide applicability. *J Appl Mech* 1951;18:293–7.
- [44] Johnson CA. Fracture statistics of multiple flaw distribution. In: Bradt RC, Evans AC, Hasselman DPH, Lange FF, editors. *Fracture mechanics of ceramics 6*. New York, USA: Plenum Press; 1983. p. 365–85.
- [45] Landel RF, Nielsen LE. *Mechanical properties of polymer and composites*. second ed. United States: CRC Press; 1993.
- [46] Schwarz MM. *Composites materials. Properties, non-destructive testing and repair*. United States, ume 1; 1997.
- [47] Data courtesy of Vemar Helmets s.r.l., Grosseto, Italy.
- [48] Hubert P, Pousartip A. Aspect of the compaction of composite angle laminates: an experimental investigation. *J Compos Mater* 2001;35(1):2–26.
- [49] Lepore E, Bosia F, Bonaccorso F, Bruna M, Taioli S, Garberoglio G, Ferrari AC, Pugno NM. Spider silk reinforced by graphene or carbon nanotubes. *2D Mater* 2017;4(3):031013.
- [50] Kim Y, Kim Y, Lee T, Kim T, Ryu S. An extended analytic model for the elastic properties of platelet-staggered composites and its application to 3D printed structures. *Compos Struct* 2018;189:27–36.

A coupled experimental/numerical study on the scaling of impact strength and toughness in composite laminates for ballistic applications

- Supplementary Information -

Stefano Signetti^{a,b}, Federico Bosia^c, Seunghwa Ryu^b, Nicola M. Pugno^{a,d*}

^a*Laboratory of Bio-Inspired, Bionic, Nano, Meta Materials & Mechanics, Department of Civil, Environmental and Mechanical Engineering, University of Trento, via Mesiano 77, I-38123 Trento, Italy*

^b*Department of Mechanical Engineering, Korea Advanced Institute of Science and Technology, 291 Daehak-ro, Yuseong-gu, Daejeon 34141, Republic of Korea*

^c*Department of Applied Science and Technology, Politecnico di Torino, corso Duca degli Abruzzi, 10129 Torino, Italy*

^d*School of Engineering and Materials Science, Queen Mary University of London, Mile End Road E1 4NS, London, UK*

*Corresponding author: nicola.pugno@unitn.it

1. Materials and samples

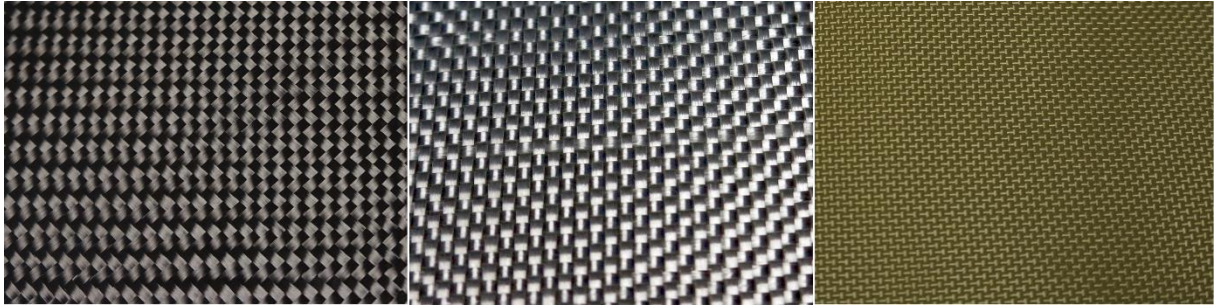


Figure S1. Picture of the textile used for the preparation of the composites. From left to right: Carbon T800, E-glass, and Twaron® (para-aramid, PA).

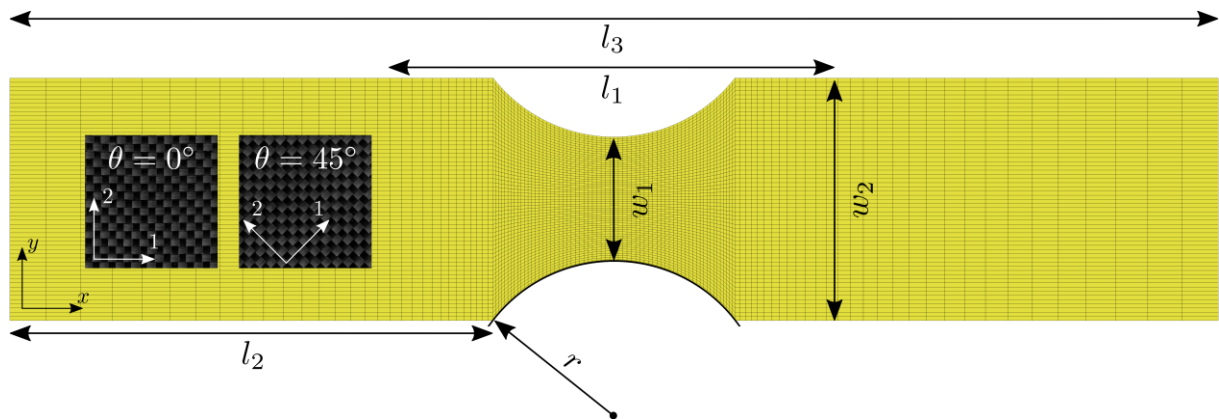


Figure S2. Dimensions of the specimens for tensile characterization (see Table S1) and visualization of the discretization of the corresponding FEM models. Analysed orientations of the woven textiles are also depicted. The global coordinate system is indicated as x - y (with the load along x direction) while 1-2 is the textile material coordinate system, oriented of an angle θ with respect to the global coordinates. For FEM simulations, the following values were used (average of experimental samples): $w_1 = 7.5$ mm , $w_2 = 15$ mm , $l_1 = 25.3$ mm , $l_2 = 29.0$ mm, $l_3 = 73.0$ mm, $r = 9.3$ mm.

Table S1. Characteristic dimensions of the tested laminate samples (S), see Figure S2 and Table 1 in the main text. Ply thickness t is determined by measuring the overall thickness of the laminates and dividing it by the corresponding number of layers.

		0°				45°				
		n	S1	S2	S3	S4	S1	S2	S3	S4
Thickness [mm]	Carbon	1	0.28	0.29	0.27	0.27	0.30	0.29	0.29	0.31
		5	1.17	1.45	1.20	1.25	1.22	1.17	1.27	1.47
		10	2.70	2.80	2.90	2.40	2.40	2.30	2.30	2.40
	E-glass	1	0.30	0.30	0.30	0.20	0.30	0.40	0.30	0.30
		5	1.00	0.90	0.90	0.90	1.00	1.50	1.30	1.00
		10	1.80	1.80	1.80	1.70	1.81	1.84	1.77	1.81
	PA	1	0.20	0.20	0.30	0.20	0.30	0.40	0.30	0.20
		5	0.90	0.90	1.00	0.90	0.90	0.90	0.90	0.80
		10	2.70	2.70	2.60	2.50	2.40	2.60	2.30	2.40
w_1 [mm]	Carbon	1	8.2	8.4	8.4	8.1	8.7	8.4	8.3	8.4
		5	9.3	8.0	7.7	7.6	7.8	7.1	8.4	7.9
		10	6.0	6.5	6.5	6.5	7.6	8.3	5.4	6.1
	E-glass	1	7.8	8.3	7.8	7.3	7.1	7.9	7.9	7.9
		5	7.9	8.1	7.9	8.2	7.9	8.0	8.1	8.0
		10	6.8	5.9	7.3	7.4	6.5	6.6	6.3	6.5
	PA	1	7.8	6.9	7.8	7.6	7.9	8.1	8.3	7.8
		5	7.0	7.5	7.0	7.5	9.2	7.0	8.0	8.8
		10	5.5	8.5	5.9	6.0	6.6	5.4	5.9	6.4
w_2 [mm]	Carbon	1	14.5	15.1	15.0	15.8	14.8	15.1	14.1	15.0
		5	17.0	14.6	14.6	14.1	15.8	14.0	15.3	15.2
		10	13.0	12.0	14.0	13.0	13.8	14.8	11.8	12.2
	E-glass	1	14.6	15.1	15.2	14.5	14.1	15.6	16.0	14.1
		5	15.7	15.0	15.1	15.6	15.0	15.2	15.1	15.0
		10	15.4	14.6	13.6	15.7	15.4	14.8	14.7	14.9
	PA	1	15.4	14.7	14.7	15.4	14.1	15.0	15.7	15.0
		5	16.0	16.5	15.0	15.0	14.8	14.5	15.0	15.5
		10	14.5	14.8	12.0	13.0	12.0	12.5	11.3	11.6
w_3 [mm]	Carbon	1	14.5	14.3	15.4	15.6	14.7	14.3	13.9	15.2
		5	16.8	14.5	14.5	13.8	16.0	13.9	15.6	15.1
		10	12.5	12.0	14.0	12.0	13.7	15.0	11.4	12.2
	E-glass	1	14.2	15.0	15.0	14.6	14.4	15.0	16.3	14.1
		5	15.5	15.2	14.9	15.5	15.0	15.4	15.3	15.1
		10	15.0	14.2	13.7	15.7	15.5	15.0	14.6	14.9
	PA	1	15.3	14.7	14.4	15.4	14.1	15.6	15.0	15.0
		5	16.0	15.0	15.0	15.0	14.4	15.0	15.0	15.5
		10	12.5	14.8	12.4	12.8	12.7	12.7	12.7	11.6
l_1 [mm]	Carbon	1	23.0	24.1	22.8	24.7	24.3	24.8	26.3	26.9
		5	29.9	29.3	29.0	28.6	18.0	19.3	17.5	18.1
		10	19.0	18.5	18.0	18.0	21.4	24.5	23.4	22.3
	E-glass	1	23.5	23.1	20.5	23.4	25.1	22.9	23.0	23.0
		5	24.4	23.6	23.6	23.1	23.1	24.3	24.3	24.0
		10	24.3	24.3	24.6	25.4	24.0	24.0	24.0	23.4
	PA	1	15.8	16.8	18.2	18.3	23.0	24.2	24.5	30.3
		5	26.0	27.0	25.0	26.0	23.5	23.0	23.0	26.0
		10	22.0	22.0	21.2	20.6	22.0	22.3	22.0	23.1

2. FEM modelling

2.1 Mesh sensitivity analysis

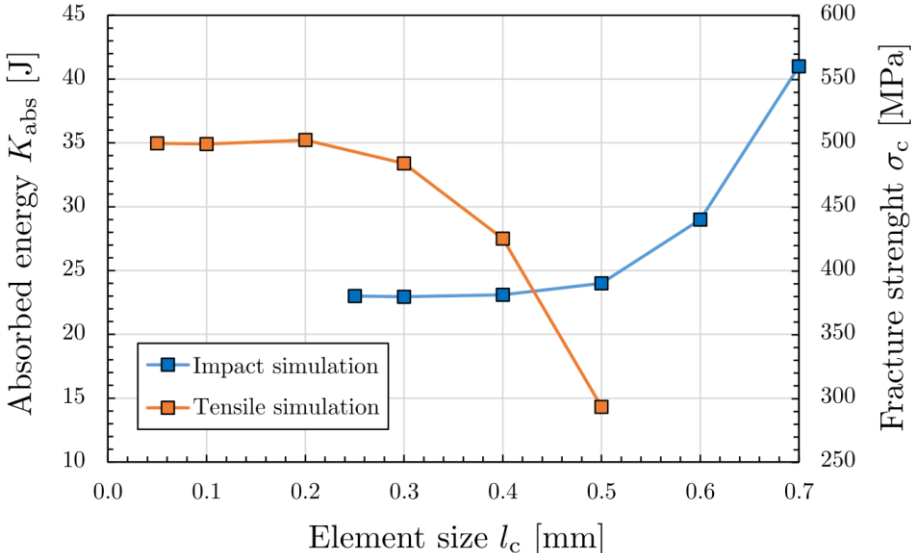


Figure S3. Convergence analysis of mesh size for tensile simulations of laminates (1 ply PA, fracture strength) and impact simulations (7 mm – 30 layers PA, absorbed energy).

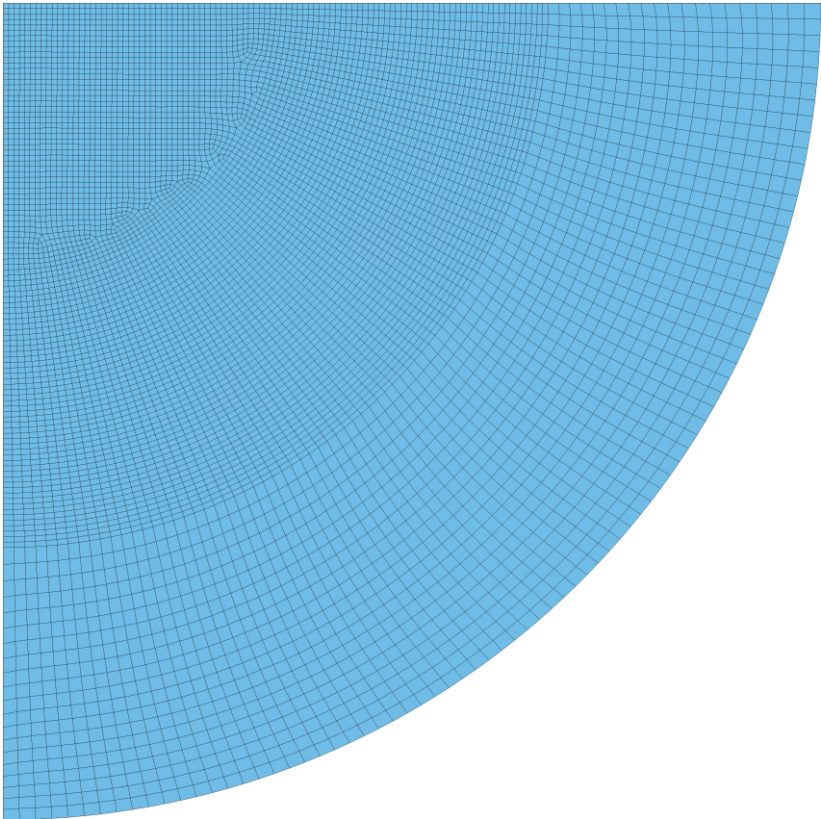


Figure S4. Discretization detail of the target in impact simulation. The characteristic in-plane size of TSHELL element is ~0.4 mm under the impact region ($< 3r$, top left) and 1.24 mm at the boundary.

2.2 Input parameters of tensile and impact simulations

Table S3. Integration scheme for tensile simulations of carbon, E-glass, and PA fibre-based composites with 1, 5, 10 plies at 0° and 45° orientation. The 6 innermost integration points (IP) are associated to the woven fabric core while the remaining outermost 4+4 are assigned to the matrix. For each IP are reported its coordinate y_G with respect to the centroid and the weighting factor wf which is the ratio of the corresponding IP thickness over the overall ply thickness and according to the laminate volume fraction (see Table 1 in the main text and Table S1).

		0°						45°					
		1 layer		5 layers		10 layers		1 layer		5 layers		10 layers	
IP		y_G	wf	y_G	wf	y_G	wf	y_G	wf	y_G	wf	y_G	wf
		[mm]		[mm]		[mm]		[mm]		[mm]		[mm]	
Carbon	1	0.12891	0.07095	0.11841	0.06583	0.12563	0.06944	0.13766	0.07458	0.11972	0.06652	0.11031	0.06117
	2	0.10922	0.07095	0.10172	0.06583	0.10688	0.06944	0.11547	0.07458	0.10266	0.06652	0.09594	0.06117
	3	0.08953	0.07095	0.08503	0.06583	0.08813	0.06944	0.09328	0.07458	0.08559	0.06652	0.08156	0.06117
	4	0.06984	0.07095	0.06834	0.06583	0.06938	0.06944	0.07109	0.07458	0.06853	0.06652	0.06719	0.06117
	5	0.05000	0.07207	0.05000	0.07890	0.05000	0.07407	0.05000	0.06723	0.05000	0.07797	0.05000	0.08511
	6	0.03000	0.07207	0.03000	0.07890	0.03000	0.07407	0.03000	0.06723	0.03000	0.07797	0.03000	0.08511
	7	0.01000	0.07207	0.01000	0.07890	0.01000	0.07407	0.01000	0.06723	0.01000	0.07797	0.01000	0.08511
	8	-0.01000	0.07207	-0.01000	0.07890	-0.01000	0.07407	-0.01000	0.06723	-0.01000	0.07797	-0.01000	0.08511
	9	-0.03000	0.07207	-0.03000	0.07890	-0.03000	0.07407	-0.03000	0.06723	-0.03000	0.07797	-0.03000	0.08511
	10	-0.05000	0.07207	-0.05000	0.07890	-0.05000	0.07407	-0.05000	0.06723	-0.05000	0.07797	-0.05000	0.08511
	11	-0.06984	0.07095	-0.06834	0.06583	-0.06938	0.06944	-0.07109	0.07458	-0.06853	0.06652	-0.06719	0.06117
	12	-0.08953	0.07095	-0.08503	0.06583	-0.08813	0.06944	-0.09328	0.07458	-0.08559	0.06652	-0.08156	0.06117
	13	-0.10922	0.07095	-0.10172	0.06583	-0.10688	0.06944	-0.11547	0.07458	-0.10266	0.06652	-0.09594	0.06117
	14	-0.12891	0.07095	-0.11841	0.06583	-0.12563	0.06944	-0.13766	0.07458	-0.11972	0.06652	-0.11031	0.06117
E-glass	1	0.12781	0.07045	0.08844	0.04392	0.08516	0.04049	0.14969	0.07885	0.11250	0.06250	0.08658	0.04201
	2	0.10844	0.07045	0.08031	0.04392	0.07797	0.04049	0.12406	0.07885	0.09750	0.06250	0.07898	0.04201
	3	0.08906	0.07045	0.07219	0.04392	0.07078	0.04049	0.09844	0.07885	0.08250	0.06250	0.07139	0.04201
	4	0.06969	0.07045	0.06406	0.04392	0.06359	0.04049	0.07281	0.07885	0.06750	0.06250	0.06380	0.04201
	5	0.05000	0.07273	0.05000	0.10811	0.05000	0.11268	0.05000	0.06154	0.05000	0.08333	0.05000	0.11065
	6	0.03000	0.07273	0.03000	0.10811	0.03000	0.11268	0.03000	0.06154	0.03000	0.08333	0.03000	0.11065
	7	0.01000	0.07273	0.01000	0.10811	0.01000	0.11268	0.01000	0.06154	0.01000	0.08333	0.01000	0.11065
	8	-0.01000	0.07273	-0.01000	0.10811	-0.01000	0.11268	-0.01000	0.06154	-0.01000	0.08333	-0.01000	0.11065
	9	-0.03000	0.07273	-0.03000	0.10811	-0.03000	0.11268	-0.03000	0.06154	-0.03000	0.08333	-0.03000	0.11065
	10	-0.05000	0.07273	-0.05000	0.10811	-0.05000	0.11268	-0.05000	0.06154	-0.05000	0.08333	-0.05000	0.11065
	11	-0.06969	0.07045	-0.06406	0.04392	-0.06359	0.04049	-0.07281	0.07885	-0.06750	0.06250	-0.06380	0.04201
	12	-0.08906	0.07045	-0.07219	0.04392	-0.07078	0.04049	-0.09844	0.07885	-0.08250	0.06250	-0.07139	0.04201
	13	-0.10844	0.07045	-0.08031	0.04392	-0.07797	0.04049	-0.12406	0.07885	-0.09750	0.06250	-0.07898	0.04201
	14	-0.12781	0.07045	-0.08844	0.04392	-0.08516	0.04049	-0.14969	0.07885	-0.11250	0.06250	-0.08658	0.04201
PA	1	0.11060	0.05833	0.09584	0.04392	0.12292	0.06786	0.13858	0.07500	0.09338	0.03929	0.11298	0.06314
	2	0.09748	0.05833	0.08772	0.04392	0.10510	0.06786	0.11608	0.07500	0.08650	0.03929	0.09766	0.06314
	3	0.08435	0.05833	0.07959	0.04392	0.08729	0.06786	0.09358	0.07500	0.07963	0.03929	0.08235	0.06314
	4	0.07123	0.05833	0.07147	0.04392	0.06948	0.06786	0.07108	0.07500	0.07275	0.03929	0.06704	0.06314
	5	0.05467	0.08889	0.05741	0.10811	0.05057	0.07619	0.04983	0.06667	0.05931	0.11429	0.04938	0.08247
	6	0.03000	0.08889	0.03000	0.10811	0.03000	0.07619	0.03000	0.06667	0.03000	0.11429	0.03000	0.08247
	7	0.01000	0.08889	0.01000	0.10811	0.01000	0.07619	0.01000	0.06667	0.01000	0.11429	0.01000	0.08247
	8	-0.01000	0.08889	-0.01000	0.10811	-0.01000	0.07619	-0.01000	0.06667	-0.01000	0.11429	-0.01000	0.08247
	9	-0.03000	0.08889	-0.03000	0.10811	-0.03000	0.07619	-0.03000	0.06667	-0.03000	0.11429	-0.03000	0.08247
	10	-0.05467	0.08889	-0.05741	0.10811	-0.05057	0.07619	-0.04983	0.06667	-0.05931	0.11429	-0.04938	0.08247
	11	-0.07123	0.05833	-0.07147	0.04392	-0.06948	0.06786	-0.07108	0.07500	-0.07275	0.03929	-0.06704	0.06314
	12	-0.08435	0.05833	-0.07959	0.04392	-0.08729	0.06786	-0.09358	0.07500	-0.07963	0.03929	-0.08235	0.06314
	13	-0.09748	0.05833	-0.08772	0.04392	-0.10510	0.06786	-0.11608	0.07500	-0.08650	0.03929	-0.09766	0.06314
	14	-0.11060	0.05833	-0.09584	0.04392	-0.12292	0.06786	-0.13858	0.07500	-0.09338	0.03929	-0.11298	0.06314

Table S4. Integration scheme for impact simulations of carbon, E-glass, and PA fibre-based composites. Each layer is made of 1 element through thickness which is in turn subdivided in 14 integration points (IP), as for tensile simulations. The 6 innermost IPs are associated to the woven fabric core while the remaining outermost 4+4 are assigned to the matrix. For each IP are reported its coordinate y_G with respect to the centroid and the weighting factor wf .

IP	Carbon 4 mm, 17 layers		E-glass 3 mm, 16 layers		PA 5 mm, 30 layers		PA 7 mm, 30 layers	
	y_G [mm]	wf	y_G [mm]	wf	y_G [mm]	wf	y_G [mm]	wf
1	0.11044	0.06125	0.08953	0.04500	0.07931	0.05015	0.10833	0.07143
2	0.09603	0.06125	0.08109	0.04500	0.07094	0.05015	0.09167	0.07143
3	0.08162	0.06125	0.07266	0.04500	0.06256	0.05015	0.07500	0.07143
4	0.06721	0.06125	0.06422	0.04500	0.05419	0.05015	0.05833	0.07143
5	0.05000	0.08500	0.05000	0.10667	0.04167	0.09980	0.04167	0.07143
6	0.03000	0.08500	0.03000	0.10667	0.02500	0.09980	0.02500	0.07143
7	0.01000	0.08500	0.01000	0.10667	0.00833	0.09980	0.00833	0.07143
8	-0.01000	0.08500	-0.01000	0.10667	-0.00833	0.09980	-0.00833	0.07143
9	-0.03000	0.08500	-0.03000	0.10667	-0.02500	0.09980	-0.02500	0.07143
10	-0.05000	0.08500	-0.05000	0.10667	-0.04167	0.09980	-0.04167	0.07143
11	-0.06721	0.06125	-0.06422	0.04500	-0.05419	0.05015	-0.05833	0.07143
12	-0.08162	0.06125	-0.07266	0.04500	-0.06256	0.05015	-0.07500	0.07143
13	-0.09603	0.06125	-0.08109	0.04500	-0.07094	0.05015	-0.09167	0.07143
14	-0.11044	0.06125	-0.08953	0.04500	-0.07931	0.05015	-0.10833	0.07143

2.3 MAT 58 input parameters

Based on the strain based failure surface, *MAT_LAMINATED_COMPOSITE_FABRIC or *MAT_058 (LS-DYNA v971 r10.1) can be used to model composite materials which have unidirectional layers, woven fibres and laminates. This model implements Matzenmiller, Lubliner and Taylor [1] theory, based on plane stress continuum damage mechanic model from Hashin [2, 3]. For the composites with woven fabrics and laminates, quadratic failure criteria are used for fibre modes and also for matrix modes, which results in smooth failure surface. Theoretical background of the models can be found in the respective papers [1-3].

Table S5. Material parameters for the epoxy matrix (*Bakelite® EPR L 1000 – set by Bakelite AG*). Strength and moduli are expressed in [GPa], density in [kg/mm³].

*MAT_LAMINATED_COMPOSITE_FABRIC_TITLE

Matrix

mid	ro	ea	eb	(ec)	prba	taul	gamma1
-	1.14E-6	3.78	3.78	3.78	0.3	0	0
gab	gbc	gca	slimt1	slimc1	slimt2	slimc2	slims
1.45	1.45	1.45	0.5	0.5	0.5	0.5	0.5
aopt	tsize	erods	soft	fs	epsf	epsr	tsmd
2	0	0.09	0	1	0	0	0.9
xp	yp	zp	a1	a2	a3	prca	prcb
0	0	0	1	0	0	0	0
v1	v2	v3	d1	d2	d3	beta	
0	0	0	0	1	0	0	
e11c	e11t	e22c	e22t	gms			
0.09	0.09	0.09	0.09	0.005			
xc	xt	yc	yt	sc			
0.0723	0.0723	0.0723	0.0723	0.0327			

Table S6. Material parameters for carbon woven textile (*GG 301 T8 Carbon T800 textile G. Angeloni s.r.l., Italy*). Strength and moduli are expressed in [GPa], density in [kg/mm³].

*MAT_LAMINATED_COMPOSITE_FABRIC_TITLE

Fibre

mid	ro	ea	eb	(ec)	prba	taul	gamma1
-	1.81E-6	85.7	85.7	85.7	0.27	0	0
gab	gbc	gca	slimt1	slimc1	slimt2	slimc2	slims
1.45	1.45	1.45	0.033	0.033	0.033	0.033	0.1
aopt	tsize	erods	soft	fs	epsf	epsr	tsmd
2	0	0.09	0.9	1	0	0	0.9
xp	yp	zp	a1	a2	a3	prca	prcb
0	0	0	1	0	0	0	0
v1	v2	v3	d1	d2	d3	beta	
0	0	0	0	1	0	0	
e11c	e11t	e22c	e22t	gms			
0.026	0.026	0.026	0.026	0.0125			
xc	xt	yc	yt	sc			
2.17	2.17	2.17	2.17	1.085			

Table S7. Material parameters for E-glass woven textile (*VV - 300 P* by G. Angeloni s.r.l., Italy). Strength and moduli are expressed in [GPa], density in [kg/mm³].

```
*MAT_LAMINATED_COMPOSITE_FABRIC_TITLE
Fibre
mid      ro      ea      eb      (ec)     prba     tau1     gamma1
-        2.54E-6  48.32   48.32   48.32    0.27     0        0
gab      gbc      gca     slimt1   slimc1   slimt2   slimc2   slims
1.45     1.45     1.45    0.073   0.073    0.073    0.073    0.1
aopt     tsize    erods   soft     fs       epsf     epsr     tsmd
2        0        0.09    0.9     1        0        0        0.9
xp       yp       zp      a1       a2       a3       prca     prcb
0        0        0       1        0        0        0        0
v1       v2       v3      d1       d2       d3       beta
0        0        0       0        1        0        0
e11c     e11t     e22c    e22t     gms
0.027    0.027    0.027   0.027    0.014
xc       xt       yc      yt       sc
0.995    0.995    0.995   0.995    0.498
```

Table S8. Material parameters for para-aramid woven textile (*Style 281* by G. Angeloni s.r.l., Italy). Strength and moduli are expressed in [GPa], density in [kg/mm³].

```
*MAT_LAMINATED_COMPOSITE_FABRIC_TITLE
Fibre
mid      ro      ea      eb      (ec)     prba     tau1     gamma1
-        1.45E-6  72.94   72.94   72.94    0.27     0        0
gab      gbc      gca     slimt1   slimc1   slimt2   slimc2   slims
1.57     1.45     1.45    0.029   0.029    0.029    0.029    0.1
aopt     tsize    erods   soft     fs       epsf     epsr     tsmd
2        0        0.009   0.9     1        0        0        0.9
xp       yp       zp      a1       a2       a3       prca     prcb
0        0        0       1        0        0        0        0
v1       v2       v3      d1       d2       d3       beta
0        0        0       0        1        0        0
e11c     e11t     e22c    e22t     gms
0.031    0.031    0.031   0.031    0.016
xc       xt       yc      yt       sc
2.52     2.52     2.52    2.52    1.26
```

2.4 Contact modelling

The adhesive contact interactions between the different plies, arising from the curing process, were implemented via a stress-based segment-to-segment tiebreak type contact (LS-DYNA - Option 6) [4], which also allows possible subsequent delamination. Considering a pair of adjacent nodes belonging to two adjacent layers, these are initially tied together and the contact interface can sustain tractions. A stress-based constitutive law is used to define the constitutive behaviour of the interface. The adhesive interface fails when the following condition is satisfied [4]:

$$\left(\frac{s_{\perp}}{\sigma_{\perp}}\right)^2 + \left(\frac{s_{\parallel}}{\sigma_{\parallel}}\right)^2 \geq 1 \quad (\text{S1})$$

where s_{\perp} and s_{\parallel} are the current normal and tangential stress between two (initially) welded interface nodes, while σ_{\perp} and σ_{\parallel} are their corresponding limit values, which, in general, are different, thus defining an elliptic domain.

Once the nodes separate the contact locally switches to a segment-to-segment penalty algorithm and the layers can mutually interact with friction. The kinetic friction law used in the contact model to compute the current friction coefficient μ assumes the following typical velocity-weakening expression [4], as a function of the local static and dynamic values μ_S and μ_D , respectively:

$$\mu = \mu_D + (\mu_S - \mu_D)e^{-c|v|} \quad (\text{S2})$$

which is a function of the modulus of the relative velocity v of the sliding nodes, and c is a decay constant. The same friction law applies for the contact between the projectile and the layers of the target.

Table S9-S11 report the contact cards for interlayer interactions used for both tensile and impact models and projectile/target interactions.

Table S9. Contact card for tiebreak type contact (inter-layer interaction).

```
*CONTACT_AUTOMATIC_ONE_WAY_SURFACE_TO_SURFACE_TIEBREAK_ID
```

ssid	msid	sstyp	mstyp	sboxid	mboxid	spr	mpr
1	2	3	3	0	0	1	1
fs	fd	dc	vc	vdc	penchk	bt	dt
0.2	0.15	0.1	0	0	0	0	0
sfs	sfm	sst	mst	sfst	sfmt	fsf	vsf
1	1	0	0	0	0	0	0
option	nfls	sfls	param	eraten	erates	ct2cn	cn
6	0.35	0.10	0.01	0	0	0	0
soft	sofscl	lcidab	maxpar	sbopt	depth	bsort	frcfrq
1	0.1	0	0	2	1	0	0
penmax	thkopt	shlthk	snlog	isym	i2d3d	sldthk	sldstf
0	0	0	0	0	0	0	0
igap	ignore	dprfac	dtstif	unused	unused	flangl	
2	1	0	0	0	0	0	

Table S10. Contact card for eroding contact between projectile and armour.

```
*CONTACT_ERODING_SURFACE_TO_SURFACE_ID
```

ssid	msid	sstyp	mstyp	sboxid	mboxid	spr	mpr
1	5000001	2	2	0	0	0	0
fs	fd	dc	vc	vdc	penchk	bt	dt
0.4	0.3	0.1	0	20	0	0	0
sfs	sfm	sst	mst	sfst	sfmt	fsf	vsf
1	1	0	0	0	0	0	0
isym	erosop	iadj					
0	1	1					
soft	sofscl	lcidab	maxpar	sbopt	depth	bsort	frcfrq
2	0.1	0	0	2	1	0	0
penmax	thkopt	shlthk	snlog	isym	i2d3d	sldthk	sldstf
0	0	0	0	0	0	0	0
igap	ignore	dprfac	dtstif	unused	unused	flangl	
2	1	0	0	0	0	0	

Table S11. Contact card for eroding contact (single surface type) for armour layers.

*CONTACT_ERODING_SINGLE_SURFACE_ID							
ssid	msid	sstyp	mstyp	sboxid	mboxid	spr	mpr
1	0	2	0	0	0	0	0
fs	fd	dc	vc	vdc	penchk	bt	dt
0.2	0.15	0.1	0	0	0	0	0
sfs	sfm	sst	mst	sfst	sfmt	fsf	vsf
1	1	0	0	0	0	0	0
isym	erosop	iadj					
0	1	1					
soft	sofscl	lclidab	maxpar	sbopt	depth	bsort	frcfrq
1	0.1	0	0	2	1	0	0
penmax	thkopt	shlthk	snlog	isym	i2d3d	sldthk	sldstf
0	0	0	0	0	0	0	0
igap	ignore	dprfac	dtstif	unused	unused	flangl	
2	1	0	0	0	0	0	

3. Supplementary results

Table S12. Mechanical and volumetric characteristics of the tested fibre bundles.

		Sample 1	Sample 2	Sample 3	Sample 4	Sample 5	Sample 6
Carbon	σ_f [GPa]	1.74	2.27	2.13	2.53	2.05	2.32
	E [GPa]	75.07	90.87	81.048	95.03	74.62	97.59
	ε_f	0.022	0.026	0.028	0.029	0.028	0.025
	ε_u	0.037	0.027	0.030	0.036	0.030	0.027
	Mass [g]	0.0698	0.0873	0.0609	0.0736	0.0642	0.0621
	l [mm]	145	178	129	159	145	150
	A [mm ²]	0.266	0.271	0.261	0.256	0.245	0.229
E-glass	σ_f [GPa]	0.94	0.99	1.02	0.98	1.04	-
	E [GPa]	35.88	54.35	44.01	49.56	57.81	-
	ε_f	0.022	0.020	0.023	0.020	0.019	-
	ε_u	0.030	0.026	0.028	0.026	0.026	-
	Mass [g]	0.0393	0.0425	0.0399	0.0402	0.0402	-
	l [mm]	140	145	140	142	137	-
	A [mm ²]	0.111	0.115	0.112	0.111	0.116	-
PA	σ_f [GPa]	2.48	2.62	2.39	2.54	2.38	-
	E [GPa]	70.22	72.28	71.83	80.16	70.22	-
	ε_f	0.031	0.031	0.031	0.030	0.031	-
	ε_u	2.55	2.39	2.48	2.61	2.55	-
	Mass [g]	0.0178	0.0198	0.0181	0.0184	0.0178	-
	l [mm]	136	138	138	140	136	-
	A [mm ²]	0.091	0.099	0.091	0.091	0.091	-

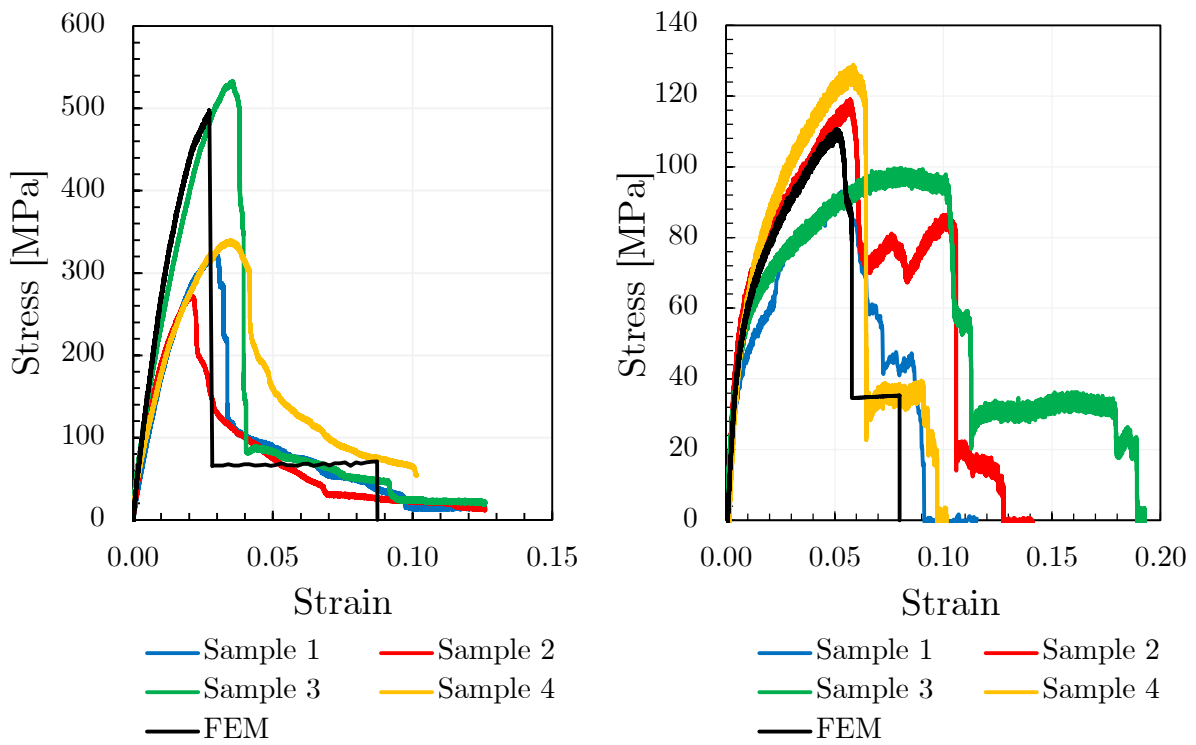


Figure S5. Stress strain curves for carbon laminate single ply from experiments and FEM simulation at 0° (left) and 45° (right) orientation.

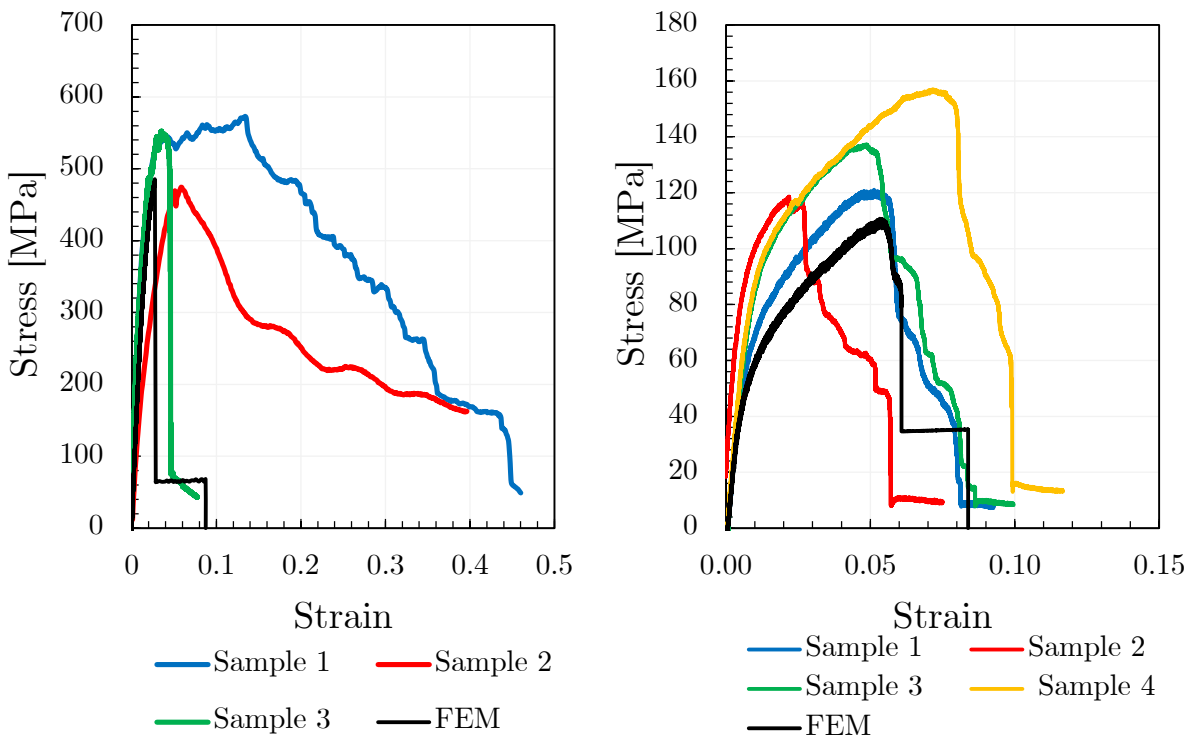


Figure S6. Stress strain curves for 5-layer carbon laminate from experiments and FEM simulation at 0° (left) and 45° (right) orientation.

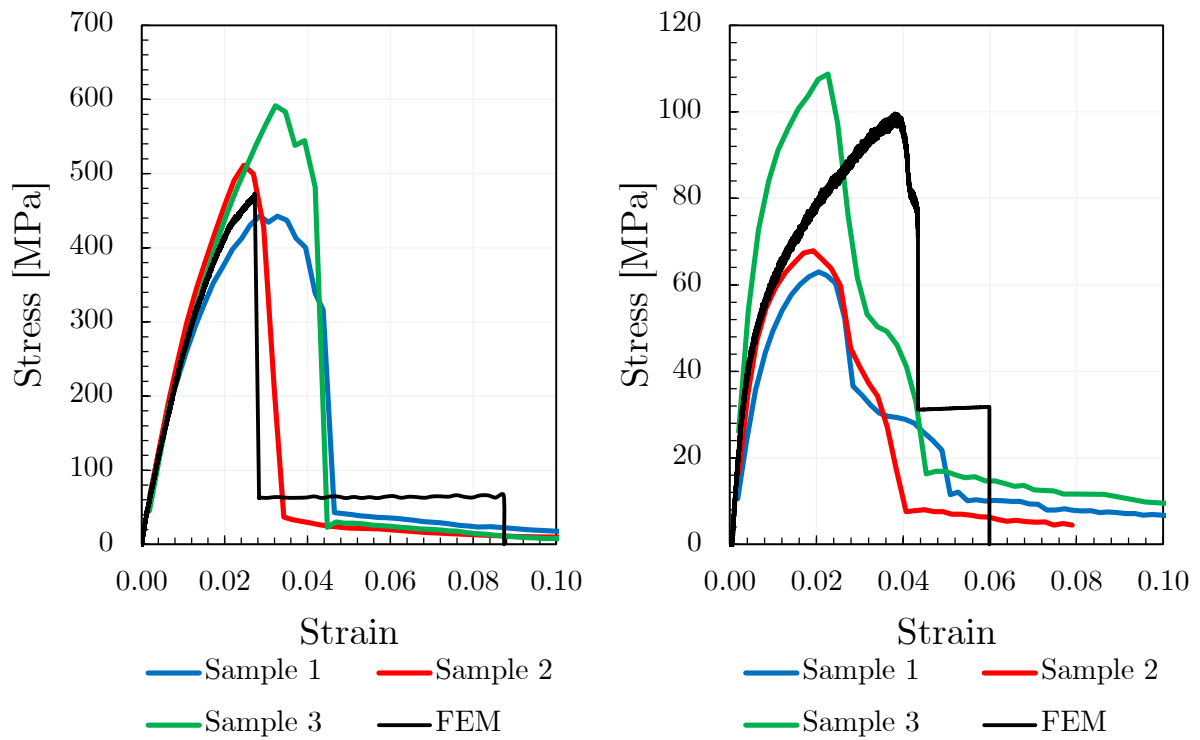


Figure S7. Stress strain curves for 10-layer carbon laminate from experiments and FEM simulation at 0° (left) and 45° (right) orientation.

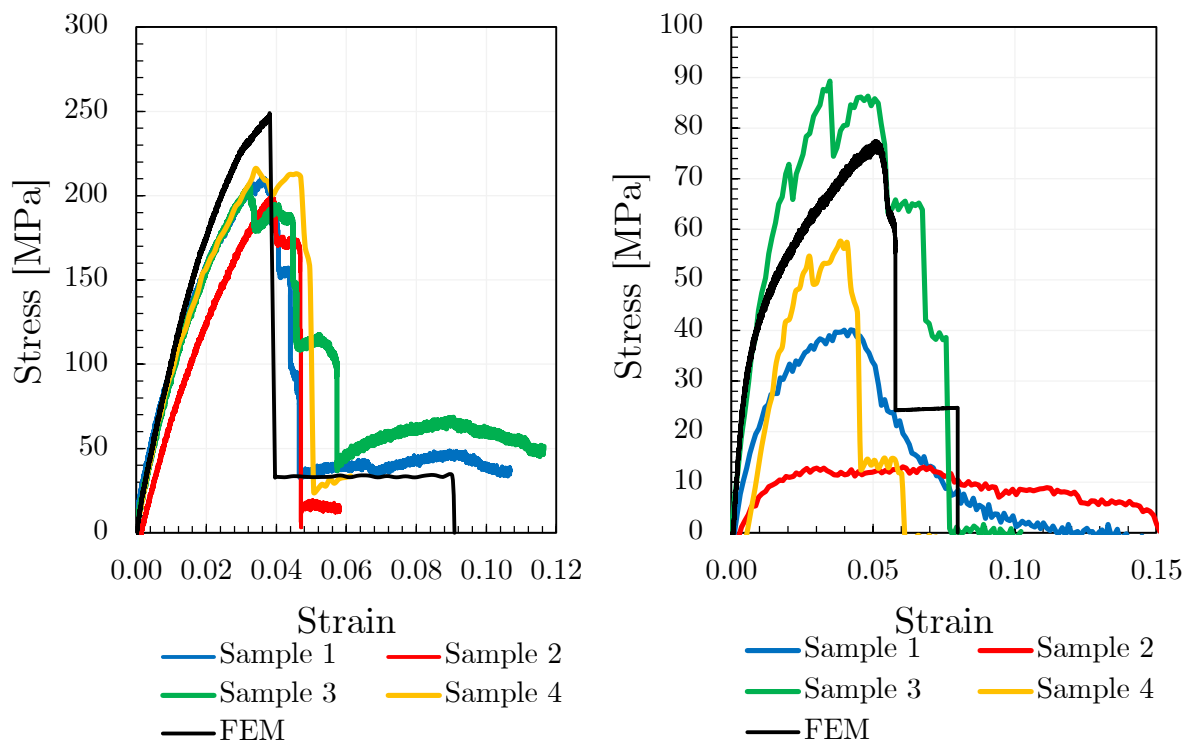


Figure S8. Stress strain curves for E-glass laminate single ply from experiments and FEM simulation at 0° (left) and 45° (right) orientation.

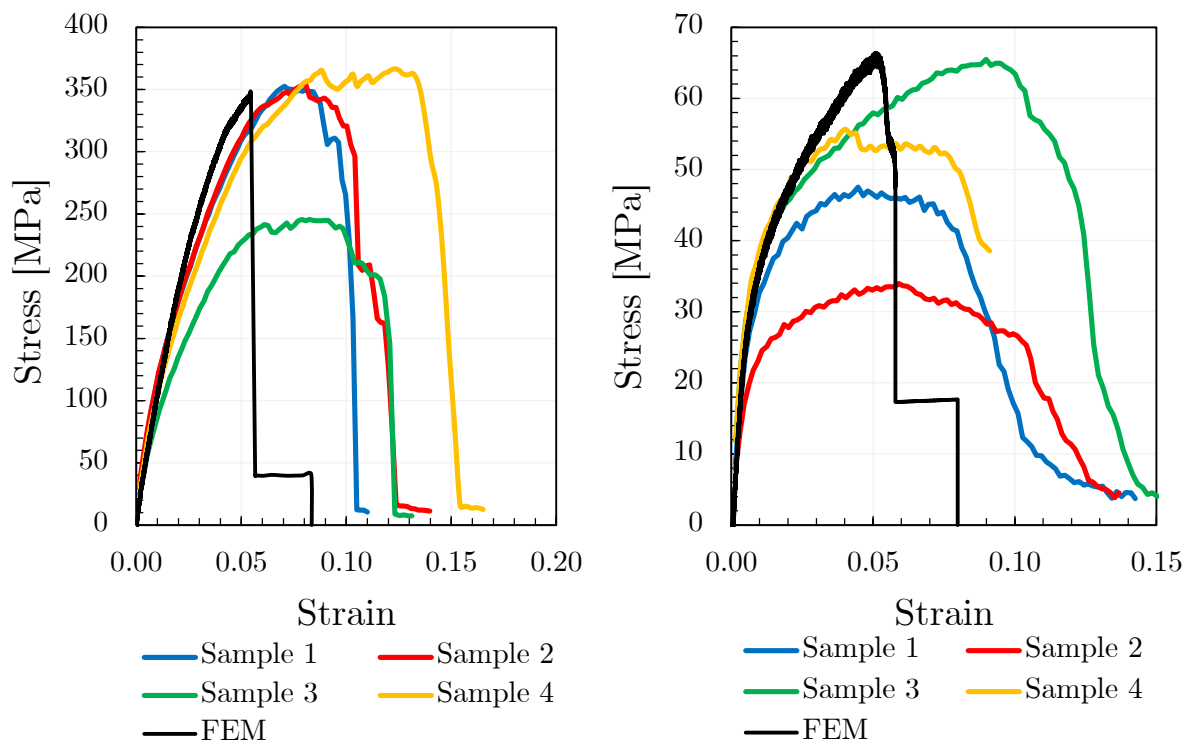


Figure S9. Stress strain curves for 5-layer E-glass laminate from experiments and FEM simulation at 0° (left) and 45° (right) orientation.

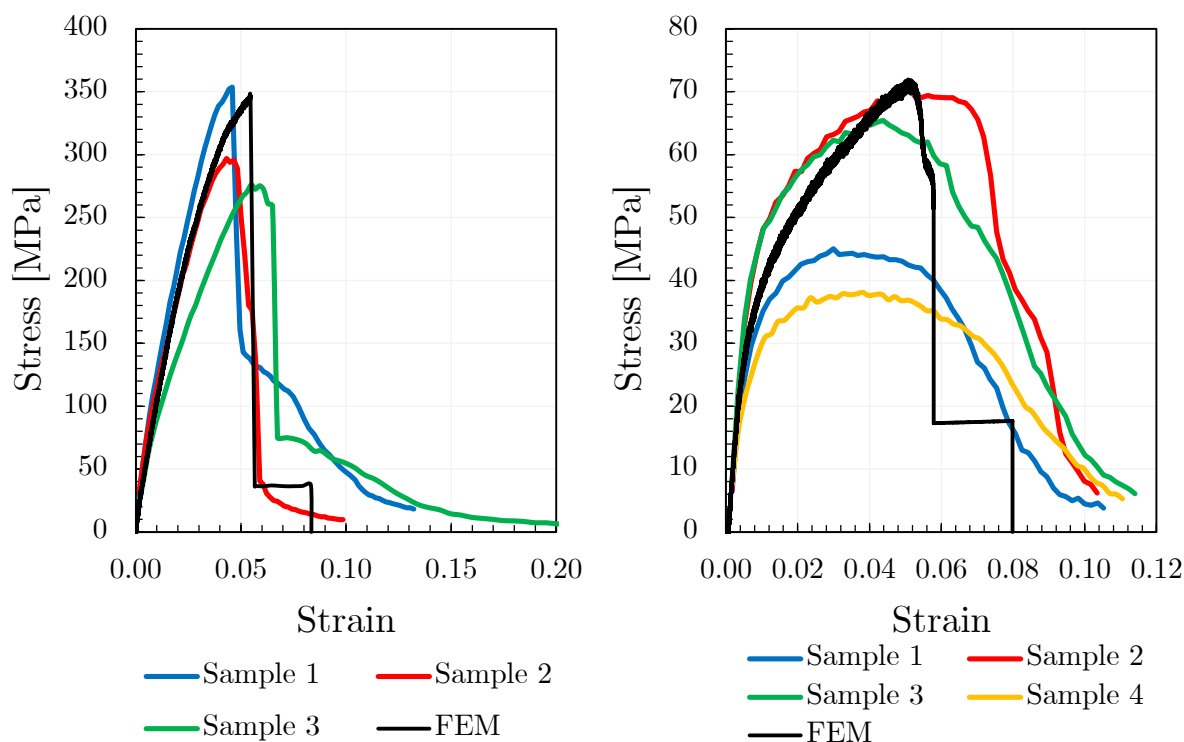


Figure S10. Stress strain curves for 10-layer E-glass laminate from experiments and FEM simulation at 0° (left) and 45° (right) orientation.

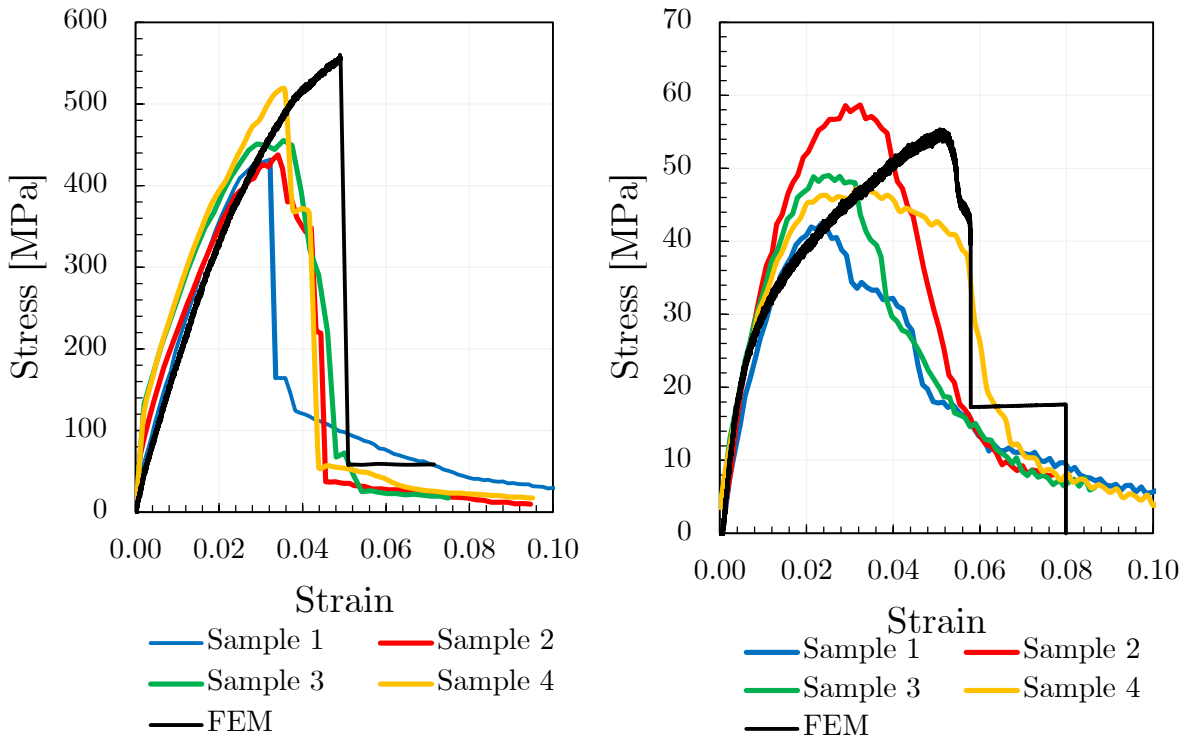


Figure S11. Stress strain curves for 5-layer PA laminate from experiments and FEM simulation at 0° (left) and 45° (right) orientation.

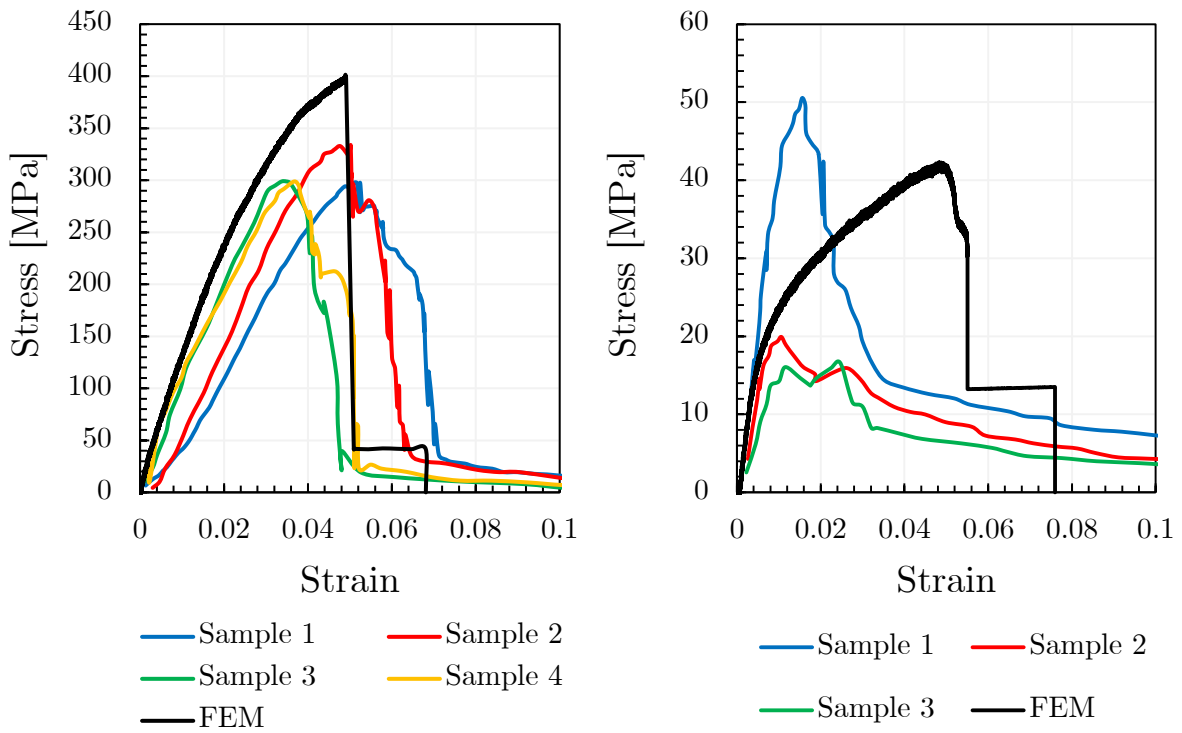


Figure S12. Stress strain curves for 10-layer PA laminate from experiments and FEM simulation at 0° (left) and 45° (right) orientation.

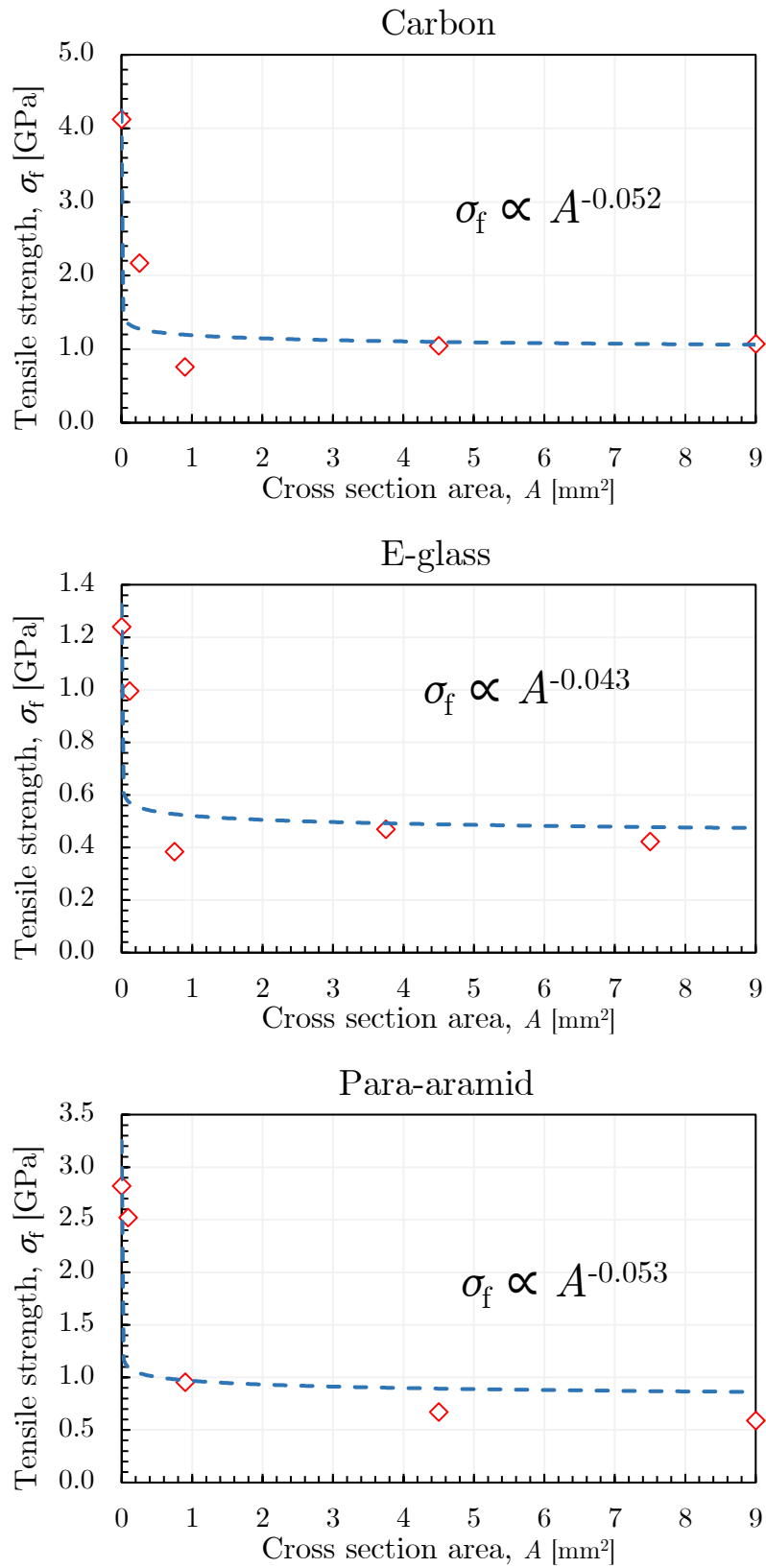


Figure S13. Scaling of reinforcement of the 3 tested materials from the single fibre, to fibre bundle, to laminate of 1, 5, and 10 layers. For the laminates the textile strength is determined from the strength of the composite ($\theta = 0^\circ$) and the corresponding fibre volume fraction (Equation (2) in the main text).

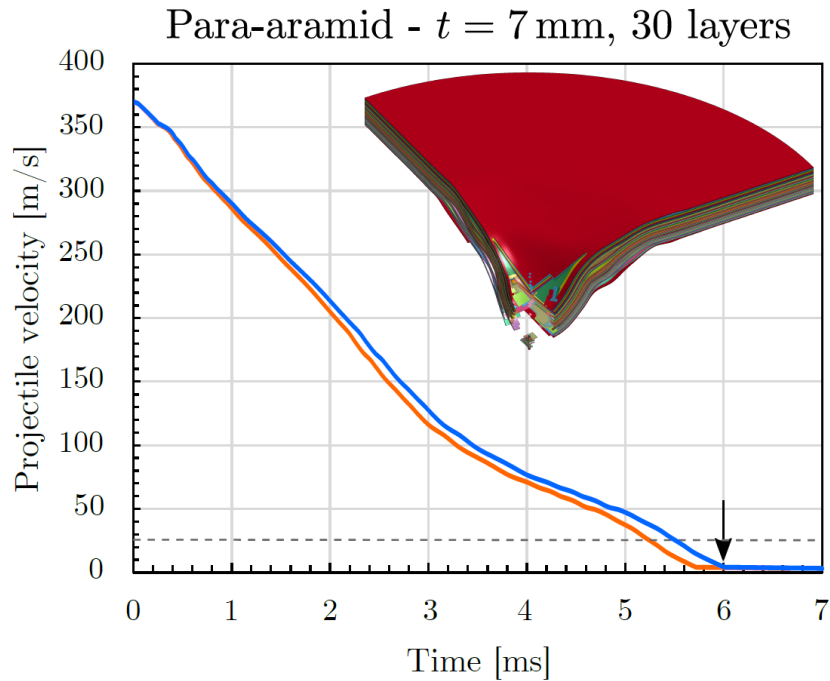


Figure S14. Comparison of the projectile velocity profile resulting from impact simulations on PA target, with (orange curve) and without (blue curve, Figure 4 in the main text) considering strain-rate effects. The maximum strain-rate measured in our impact simulations is $\sim 300 \text{ s}^{-1}$, and the scaling of mechanical properties is derived from references [5, 6].

References

- [1] Matzenmiller A, Lubliner J, Taylor RL. A constitutive model for anisotropic damage in fibre composites. *Mech. Mater.* 1995; 20(2):125-152.
- [2] Hashin Z. Failure criteria for unidirectional fiber composites. *J. of Appl. Mech.* 1980; 47(2):329-334.
- [3] Chang F, Chang K. A progressive damage model for laminated composites containing stress concentrations. *J. Compos. Mater.* 1987; 21(9):834-855.
- [4] Hallquist J. *LS-DYNA Theory Manual*. Livermore Software Technology Corporation, CA, USA, 2006.
- [5] Wang Y, Xia Y. The effect of strain rate on the mechanical behavior of Kevlar fibre bundles: an experimental and theoretical study. *Compos. Part A-Appl. S.* 1998; 29(11):1411-1415.
- [6] Gilat A, Goldberg RK, Roberts GD. *Strain Rate Sensitivity of Epoxy Resin in Tensile and Shear Loading*. NASA report NASA/TM-2005-213595, 2005.